

Separation of Diffractions from Reflections by the Double Square Root Operator

Sanchya Rathy



**Master thesis
Geophysics
60 credits**

**Department of Geoscience
The Faculty of Mathematics and Natural Science**

UNIVERSITY OF OSLO

Spring 2020

«Separation of diffractions from reflections by the Double Square Root Operator»

Sanchya Rathy

© 2020 Sanchya Rathy

Separation of diffractions from reflections by the Double Square Root Operator

Supervisor: Leiv Jacob Gelius

<http://www.duo.uio.no/>

Printed: Representeren, University of Oslo

Abstract

Diffractions can provide information about small scale heterogeneities. However, in many cases, the diffracted energy is masked by the stronger reflections. Thus, techniques for separating diffractions from reflections are desired in seismic processing. In this thesis, different approaches to diffraction enhancement are discussed, but with special emphasis put on the Double Square Root (DSR) operator employed here.

A complete workflow has been established for diffraction separation and imaging based on standard seismic reflection data. In this work, controlled data sets of various complexity have been employed to test out this procedure. Data from two simpler models were calculated using a finite-difference code from the NUCLEUS package of PGS. In addition, controlled data associated with the well-known SIGSBEE 2A model was employed. This latter model represents a complex subsurface including a salt body. For all models investigated, diffraction separation seemed to work well employing the proposed workflow.

Acknowledgment

I would first like to thank my supervisor Leiv Jacob Gelius for the guidance and support throughout the thesis period. He has helped me with the basic understanding that is required to complete this project. He always made me focus on my project, and I am thankful to my supervisor for that.

Secondly, I will thank Ph.D. student Vemund Stenbekk Thorkildsen, for his kindness and helping mind. He has helped me with the understanding of the software and all programming. I sincerely appreciate all the help and advice. I can not put words on how much he has helped me, even in this stressful time of the Coronavirus. Thorkildsen has been an enormous support to me.

A special mention goes to my family. I would like to thank my mother, Rathy Krishnapillai, and my siblings Saaruja and Lavanyan, for their support and their continuous encouragement to ensure that I stayed on track during the entire period.

I would also like to thank Karl Johan Ullavik Bakken (Geoscience supervisor) for the immense support I got in this hard period. He has helped me a lot during the two years I have studied at the University of Oslo. I sincerely appreciate the talks and support that I have gained from him.

Sanchya Rathy,
July 2020

Contents

1	Introduction and motivation	1
1.1	Objective and thesis structure.....	1
2	Methods.....	3
2.1	Common Mid-Point (CMP) and Normal Move-Out (NMO)	3
2.2	Common Reflection Surface (CRS) method	4
2.3	Common Diffraction Surface (CDS).....	7
2.3.1	CDS	7
2.3.2	Analytic link.....	7
2.4	Double Square Root equation (DSR)	9
2.5	Pragmatic search.....	10
2.6	Coherency measure.....	10
2.7	Post-stack enhancement (combined stacks)	11
2.8	Post-stack time-migration.....	12
2.8.1	The Kirchhoff migration method	12
3	Workflows, apertures, and search parameters.....	14
3.1	Diffraction stacking - workflow	14
3.2	Apertures (δ) – general observations	17
3.3	Choice of search parameters.....	17
4	Software demonstration using controlled data	18
4.1	Generating controlled data using Nucleus+.....	18
4.2	Diffraction-enhancement using MATLAB code.....	23
4.3	Post-stack time-migration using code from CREWES.....	28
5	Diffraction separation results – controlled-data studies	31
5.1	Simple point-scatterer model.....	31
5.1.1	Definition of model parameters.....	31
5.1.2	Basic steps in diffraction-enhancement.....	32

5.1.3	Combined stacks	36
5.1.4	Post – stack migration	38
5.2	SIGSBEE 2A	40
5.2.1	Workflow	42
5.2.2	Separation results	46
6	Discussion	53
6.1	Simple scattering model	53
6.2	SIGSBEE 2A	54
7	Conclusions and further work	55
8	References	56
APPENDIX		I
APPENDIX A		II
APPENDIX B		IV
APPENDIX C		IX

LIST OF FIGURES

Figure 1-1: A comparison between (a) CDS and (b) DSR stacked sections (see areas marked with the white arrow to note the differences). Images were taken from (Facciopieri et al., 2016) 2

Figure 2-1: CMP sorting with source and receiver pairs with a common depth point. Figure from (Schlumberger, 2020). 4

Figure 2-2: Definition of the two CRS wavefronts: NIP wave in red and the normal wave in green. The propagation is along the normal ray shown in blue. Figure from (Mann et al., 2007)..... 6

Figure 2-3: Schematics of the analytical link between t_0 (twt), v_0 , and R_{NIP} in case of a homogenous velocity v_0 . Based on the figures from (Thorkildsen, 2019; Javed, 2012) 7

Figure 2-4: Schematics of diffraction summation migration. From (Gazdag & Sguazzero, 1984)..... 12

Figure 3-1: workflow for diffraction-stacking and imaging. Based on (Thorkildsen, 2019)... 16

Figure 4-1: Flow chart of the main steps in FD-modelling in NUCLEUS+ 19

Figure 4-2: Example of a vessel plot in 3D. The blue lines are the six streamers, and the two red dots represent the sources..... 19

Figure 4-3: a 2D survey with the minimum(x_1) and maximum(x_2) offset. The red dot indicates the source and the green part, the receivers. 20

Figure 4-4: P-wave velocity model. 21

Figure 4-5: a) the strong diffractor at $x=5000m$ and $850m$ depth b) zoomed-in version of the scatterer showing the step-like pattern. 22

Figure 4-6: a) Example of source gathers output from finite-difference modeling with direct wave. b) The same source gathers after removal of direct wave. 22

Figure 4-7: A selection of source gathers after white-noise addition..... 23

Figure 4-8: Left: The optimal velocity field output from semblance analysis and right: corresponding semblance panel. 24

Figure 4-9: conventional NMO stack..... 24

Figure 4-10: Plot of A parameter (left) and updated C parameter (right) for aperture Δm 1200 and Δh 500..... 25

Figure 4-11: Semblance panel output from midpoint search for an aperture of Δm 1200 and Δh 500. 25

Figure 4-12: Plot of parameter A (left) and C(right) after multi-domain refinement for aperture Δm 1200 and Δh 500.	26
Figure 4-13: The semblance panel after the multi-domain refinement for aperture Δm 1200 and Δh 500.	26
Figure 4-14: DSR stack before thresholding for aperture Δm 1200 and Δh 500.	27
Figure 4-15: DSR stack after thresholding (Vemund) for apertures Δm 1200 and Δh 500. ...	27
Figure 4-16: DSR stack after thresholding (Endrias) for apertures Δm 1200 and Δh 500.....	28
Figure 4-17: image obtained with a migration apertures of 500m. Left: «Endrias» thresholding and right: «Vemund» thresholding of input.	29
Figure 4-18: image obtained with a migration aperture of 2500m. Left: «Endrias» thresholding and right: «Vemund» thresholding of input.	29
Figure 4-19: image obtained with a migration aperture of 5000m. Left: «Endrias» thresholding and right: «Vemund» thresholding of input.	30
Figure 5-1: a) Overall model (velocity color-coded) and b) zoomed version of the diffraction points.	31
Figure 5-2: Example of a source gather output from FD-modelling.....	32
Figure 5-3: Velocity model (left) and the corresponding semblance plot (right)	33
Figure 5-4: NMO stack	33
Figure 5-5: A parameter panel (left) and C parameter panel (right) for apertures Δm 1500 and Δh 500	34
Figure 5-6: Semblance in the midpoint.....	34
Figure 5-7: Semblance in midpoint after multi-domain refinement	35
Figure 5-8: Brute-force diffraction-enhanced stack for apertures Δm 1500 and Δh 500.....	36
Figure 5-9: Diffraction stack after thresholding. «Vemund» option (left) and «Endrias» option (right).....	36
Figure 5-10: NMO-stack ($\alpha = 0$).....	37
Figure 5-11: Combined stacks corresponding to $\alpha = 0.3$. «Vemund» option (left) and «Endrias» option (right)	37
Figure 5-12: Combined stacks corresponding to $\alpha = 0.8$. «Vemund» option (left) and «Endrias» option (right)	38
Figure 5-13: Time-migrated NMO-stack.	39
Figure 5-14: Migrated versions of the diffraction-enhanced stacks in Fig.5-9 with apertures of Δm 1500 and Δh 500. «Endrias» option (left) and «Vemund» option (right).....	39

Figure 5-15 Migrated versions of the combined stacks ($\alpha=0.8$) in Figure 5-12. «Vemund» option (left) and «Endrias» option (right)	40
Figure 5-16: Velocity-depth model of the SIGSBEE 2A dataset. The black arrow indicates the salt structure and only the data on the right side of the black line is used. Note also that the depth is in feet. From (SMAART JV, 2001).....	41
Figure 5-17: Workflow of the SIGSBEE dataset. Note: the only differences from the workflow in Figure 3-1 are represented by the blue boxes.	43
Figure 5-18: Stacking velocity field before (left) and after (right) applying smoothing. Note: the velocities are in feet in these plots.....	44
Figure 5-19: NMO-stack based on raw stacking velocities.	44
Figure 5-20: NMO-stack based on smoothed stacking velocities.....	45
Figure 5-21: NMO-stack for selected part of the model (left) and corresponding stacking-velocity model of the interest area.	46
Figure 5-22: Parameter A (left), C (middle) and semblance (right) from midpoint search	47
Figure 5-23: Semblance in midpoint after multi-domain refinement for SIGSBEE model.....	48
Figure 5-24:DSR stack before thresholding for SIGSBEE data	49
Figure 5-25: DSR stacks after thresholding. (left) «Vemund» option and (right) «Endrias» option.....	49
Figure 5-26: Migration of diffraction-enhanced stack (left) and (right) combined stack – «Endrias» option	51
Figure 5-27: Migration of diffraction-enhanced stack (left) and combined stack (right) – «Vemund» option.....	52

List of Tables

Table 4-1: Survey design parameters	20
Table 4-2: choice of migration parameters.	29
Table 5-1: Key model parameters of the SIGSBEE 2A dataset. (Bauer, 2014)	41

1 Introduction and motivation

The main focus of seismic processing is on reflection data. However, reflections do not adequately give information about small-scale features (Thorkildsen, 2019). On the contrary, diffractions can provide information about faults, near-surface scattering, pinch outs, or any sudden changes in facies (Kanasewich & Phadke, 1988). This kind of information can often represent target areas or, in other words, the hydrocarbon traps. It is, therefore important to obtain as much information as possible from the seismic data, and the potential use of diffracted energy is investigated in this thesis work. It should be mentioned that diffractions besides carrying information about small-scale features also are sensitive to velocities and can, therefore, be used to build an improved velocity model (Thorkildsen, 2019).

The main challenge regarding the use of diffractions is that most diffracted energy is weak. This implies that the stronger reflections will often mask the underlying diffractions. Thus, one needs to apply special techniques to enhance the weaker diffractions and separate them from the reflected energy.

1.1 Objective and thesis structure

To make use of the diffractions, the energy of it needs to be separated from the reflections as briefly discussed above. Therefore, the main objective of this thesis is to investigate a proper separation technique so that the weak diffractions get visible and can be employed to image high-resolution features.

The method used for separation in this thesis is based on traveltimes stacking, which can be implemented either by Common Diffraction Surface (CDS) or Double Square Root (DSR) equation. The Common Reflection Surface (CRS) method improves the signal to noise ratio of noisy data (Waldeland et al., 2018). The CDS method is an extension of CRS valid for diffractions only. CDS is computational heavy when used in combination with semblance as a coherency measure (Asgedom et al., 2012a). The computational time may, however, be reduced by introducing simplified analytical expressions between parameters and thereby decrease the data volume of the search. In this thesis work, the DSR stacking operator will be employed in the data analyses. The concept of the CDS operator will also be discussed from a theoretical point of view since it forms the basis of the efficient search strategy employed using DSR. The superior performance of the DSR operator compared to the more conventionally used CDS

operator has been well documented in the literature (Facciopieri et al., 2016). Figure 1-1 shows a comparison between the CDS (a) and the DSR (b) operator in case of a field data study. It can easily be seen from the figure that DSR performs best. DSR has better separation of events and also no residual reflections (see sections marked with white arrows).

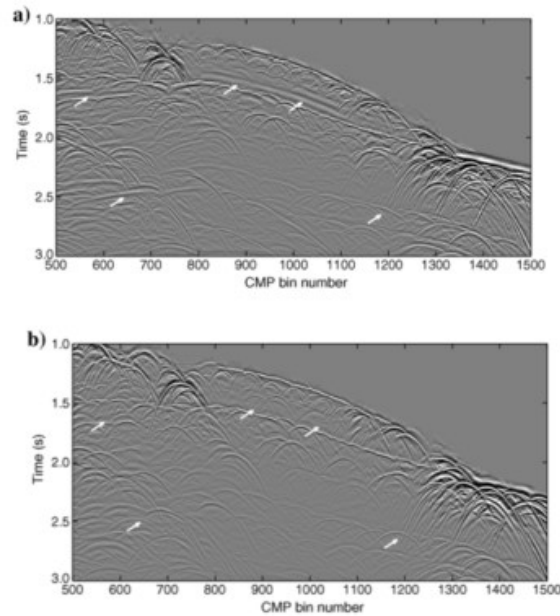


Figure 1-1: A comparison between (a) CDS and (b) DSR stacked sections (see areas marked with the white arrow to note the differences). Images were taken from (Facciopieri et al., 2016)

This thesis is organized as follows. Chapter 2 gives a brief overview of the main theory employed in the thesis work. The stacking operators of the DSR and CDS techniques are introduced and discussed. Chapter 3 gives an overview of the basic workflow of diffraction separation, including a discussion on how to select data apertures, and search parameters. The corresponding software (codes or packages) employed in the workflow introduced in Chapter 3 are discussed in Chapter 4. A simple controlled data example is used to demonstrate each of the computational steps and use of the specific software. In Chapter 5, two controlled data cases are analyzed. The first example is used to demonstrate the possible use of a weighted stack of the conventional stack and the diffraction separated stack. In this way, weaker diffractions can be enhanced when combined with reflections. The second example is based on controlled data from the SIGSBEE 2A model. This is a complex model including a salt structure, thus represents a more realistic and challenging case of diffraction separation. Both the conventionally stacked data, as well as the diffraction-separated data, are post-stack time-migrated as well. Finally, Chapter 6 and 7 give an overall summary of the results obtained and with some conclusions and suggestions to further work.

2 Methods

The main idea is to enhance the often weak diffractions where reflections are present. Common Diffraction Surface (CDS), and Double Square Root (DSR) are two operators that can be used to separate diffractions from reflections. It is necessary to have a basic understanding of these diffraction tailored operators. In addition to the mentioned operators, the Common Reflection Surface (CRS) operator is also discussed in this method section. The various operators have all in common that they represent Taylor expansions of the various traveltimes equations. It is useful to start with the more conventional Common Mid-Point (CMP) sorting (Section 2.1) to understand the CRS operator. Unlike CMP, the CRS operator represents data associated with a reflection surface, thus also include data with varying midpoint coordinates (multiple CMP gathers) (Section 2.2). It is further demonstrated that the CDS operator represents an extension of CRS tailored for diffractions. Based on strategies developed for the CDS operator (Section 2.3), the more optimal diffraction-separation operator DSR is introduced and discussed (Section 2.4). Sections 2.5 and 2.6 give the basics of the semblance-based parameter searches associated with the DSR operator. Finally, Sections 2.7 and 2.8 deal with post-processing of diffraction-enhanced data (including post-stack time-migration).

2.1 Common Mid-Point (CMP) and Normal Move-Out (NMO)

Common Mid-Point (CMP) sorting is central in basic seismic processing, forming new families of data (CMP gathers) from seismic input data (source gathers). The primary purpose of this method is to obtain an improved stack of the underground from repeated measurements after traveltimes corrections. The first step is to sort source and receiver pairs that share the same midpoint into a gather (Faccipieri et al., 2016). Figure 2-1 demonstrates the principle of simple CMP sorting. In this case, since the reflector is horizontal, all source and receiver pairs contain reflections from the same depth point (i.e a CDP gather).

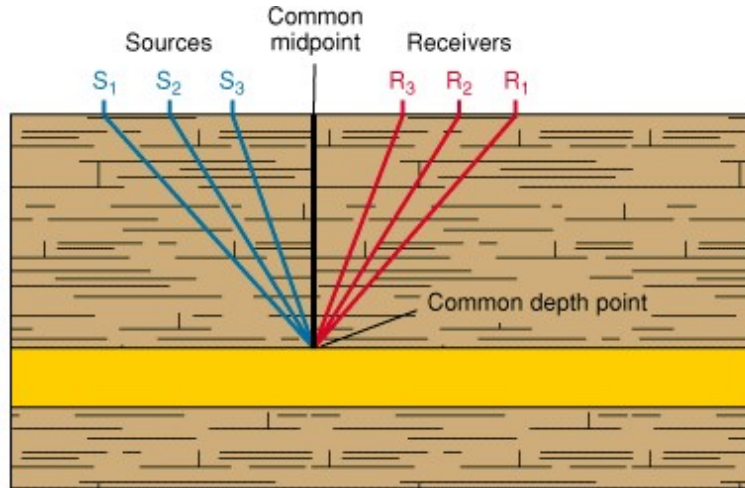


Figure 2-1: CMP sorting with source and receiver pairs with a common depth point. Figure from (Schlumberger, 2020).

For a horizontally layered earth model, the traveltime separation between the source and the receivers for a reflection relative of zero-offset (ZO) is known through the Normal Move-Out (NMO) (Thorkildsen, 2019). It represents a correction applied to data sorted in a CMP gather for a horizontally layered earth model (Thorkildsen, 2019). The Normal Move-Out correction is described by a second-order traveltime equation given as,

$$t^2(h) = t_0^2 + \frac{4h^2}{v_{nmo}^2} \quad (2.1)$$

where t_0 is the zero offset travel time, h is the half-offset, and V_{nmo} is the normal move-out velocity (Waldeland et al., 2018). In practice, V_{nmo} is approximated by the stacking velocity determined during the velocity analysis. Stacking represents the summation of the traces in each CMP gather after NMO correction.

As mentioned earlier, the CMP method is frequently in use in basic seismic signal processing. Even though it is commonly in use, it has some weaknesses. When data has been sorted into CMP gathers, the dip or curvature of a reflector can not be accounted for. The CMP/NMO method is used for generating ZO stacks. However, in ease of relatively noisy data, the CRS technique can be employed. (Thorkildsen, 2019).

2.2 Common Reflection Surface (CRS) method

The Common Reflection Surface (CRS) stack shares the same basic concepts as the CMP stack (Mann et al., 2007). However, this method differs from the CMP technique by considering multiple CMP gathers. Since CRS uses more traces, this leads to a natural increase in the signal to noise ratio compared to a conventional stack (Mann et al., 2007). Besides improving the

signal to noise ratio (S/N) for reflection stacks, the method also serves as the starting point for the DSR operator used to separate diffractions from reflections (Section 2.3). The CRS method is based on the second order-squared traveltimes, as shown in Equation 2.2. It describes the traveltimes of a paraxial ray in the vicinity of a reference (normal) ray (Dell & Gajewski, 2011).

The NMO-equation used for a single CMP gather is a one parametric second-order traveltimes equation. By including new data along the (relative) midpoint coordinate in CRS, the dependence on the reflector curvature can be included as well (Hertweck et al., 2007). In the common-mid point section, this parameter will combine as one parameter with the NMO velocity. In Equation 2.2, the effect of curvature is represented through the curvature-moveout (CMO) velocity (V_{cmo}) and depends on the NMO velocity (Mann et al., 2007). Unlike the case of CMP, the CRS traveltimes equation now depends on three parameters and represents a traveltimes surface instead of a single curve as in the CMP gather. The squared of the CRS traveltimes equation can be expressed as,

$$t^2(\Delta m, h) = t_0^2 + \frac{h^2}{v_{nmo}^2} + \frac{\Delta m^2}{v_{cmo}^2} + 4t_0p\Delta m + 4p^2\Delta m^2, \quad \Delta m = m - m_0 \quad (2.2)$$

where v_{nmo} is the normal move-out velocity, v_{cmo} is the curvature moveout velocity, p is the horizontal slowness (slope parameter) at the surface, and t_0 is the zero offset traveltimes. The quantity $\Delta m = m - m_0$ is known as the relative midpoint coordinate expressed as the difference between the zero-offset reference point m_0 and the midpoint m of the paraxial ray. In other words, it represents the midpoint displacement from the central CMP gather that is under consideration (Hertweck et al., 2007). For $\Delta m=0$, Equation 2.2 simplifies to Equation 2.1.

Equation 2.2 is an extension of the hyperbolic CMP stack along the relative midpoint and is still a second-order equation of traveltimes. This equation contains terms describing the dip of the reflection events and reflector curvature and represents the reflection traveltimes for all points on a common reflection surface (Mann et al., 2007). In summary, this equation depends on both offset and relative midpoint. Due to the paraxial ray assumption, the aperture in offset and midpoint must be limited. An alternative way to write Equation 2.2 is as follows,

$$t^2(\Delta m, h) = (t_0 + A\Delta m)^2 + B\Delta m^2 + Ch^2 \quad (2.3)$$

which is the corresponding data space representation of the traveltimes surface; likewise, Equation 2.2 is a model-space representation. The unknown parameters A, B, and C are

determined using a semblance measure as described in Section 2.5. A way to extend the CRS method to handle diffractions is by linking the parameters with model quantities (Thorkildsen, 2019):

$$A = \frac{2\sin\alpha}{V_0} \quad B = \frac{2t_0\cos^2\alpha R_N}{V_0} \quad C = \frac{2t_0\cos^2\alpha R_{NIP}}{V_0} \quad (2.4)$$

where V_0 is the velocity of the uppermost layer. In CRS stacking, the parameters α , R_{NIP} , and R_N are known as CRS attributes in model space (Thorkildsen, 2019). They represent respectively the take-off angle and two wavefronts associated with the reference ray, as shown in Figure 2-2. The model space corresponds to the depth domain, with CRS parameters being wavefront curvatures and emergence angle. However, in data space, the parameters will be stacking parameters A, B, and C in the time domain (Mann et al., 2007).

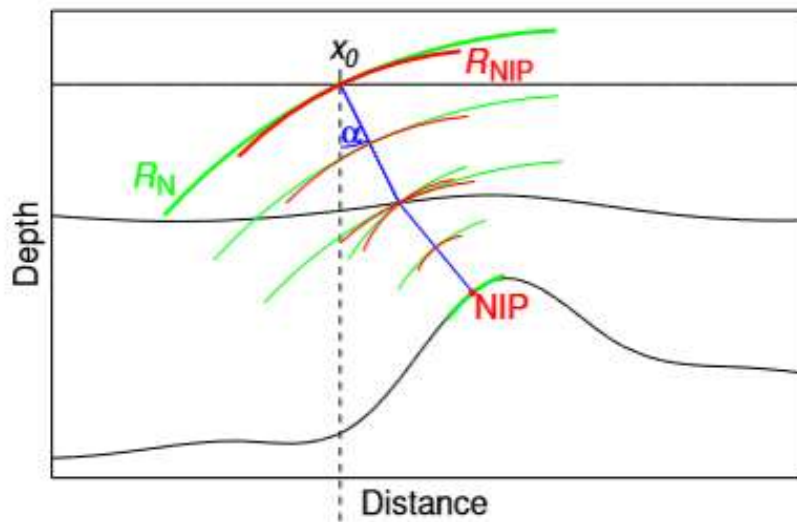


Figure 2-2: Definition of the two CRS wavefronts: NIP wave in red and the normal wave in green. The propagation is along the normal ray shown in blue. Figure from (Mann et al., 2007).

In Equation 2.4, R_{NIP} (red in Figure 2-2) is the wavefront of a wave starting from a normal incident point (NIP), and R_N (green in Figure 2-2) is the wavefront associated with an exploding reflector around the same normal incident point (Asgedom et al., 2011). The CRS operator can give a significant increase in the signal to noise ratio (S/N) due to additional stacking along midpoint (Mann et al., 2007).

2.3 Common Diffraction Surface (CDS)

2.3.1 CDS

The Common Reflection Surface method introduced in Section 2.2 is tailored for reflections but can be further extended to the case of diffractions. By letting the reflection surface shrink to a point, the wavefronts R_N and R_{NIP} will be equal in the limiting case (Facciopieri et al., 2016). Again, this limiting case implies that Equation 2.3 transforms to Equation 2.5,

When $R_N = R_{NIP}$ gives $B=C$,

$$t^2(\Delta m, h) = (t_0 + A\Delta m)^2 + C\Delta m^2 + Ch^2 \quad (2.5)$$

The critical parameters are the apertures (ranges) in midpoint and offset employed when determining the parameters in Equation (2.5) using a semblance analysis. In the case of diffraction separation, the use of a larger aperture in midpoint than an offset is necessary.

Determining the parameters A and C independently using a full search can be computationally demanding. It is, however, possible to derive an analytical link between A and C (Thorkildsen, 2019), which leads to a faster algorithm and a more constrained solution space (Subsection 2.3.2).

2.3.2 Analytic link

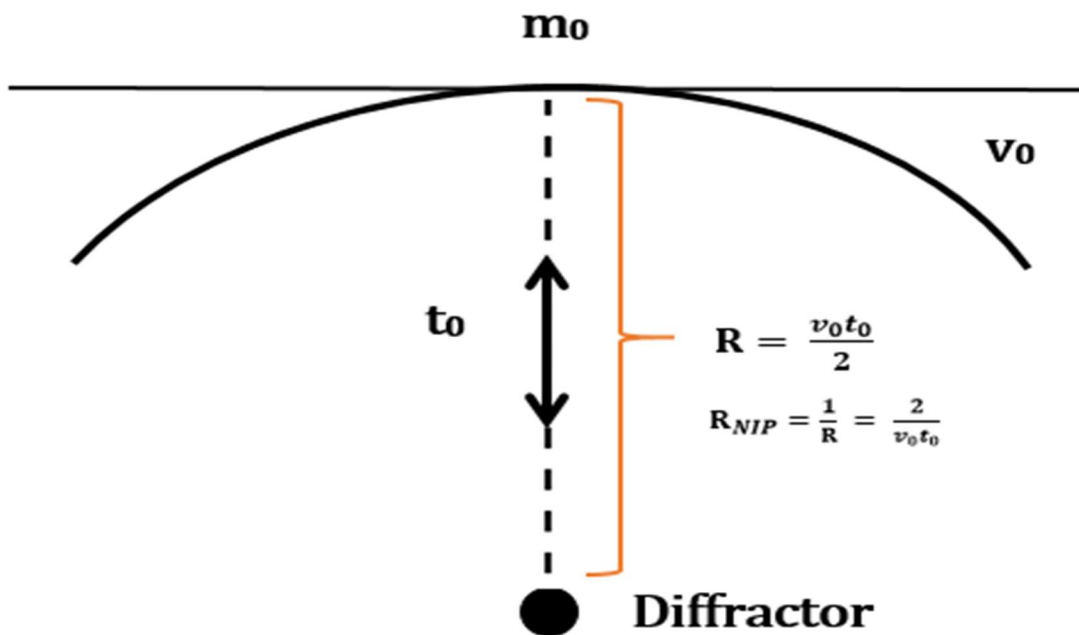


Figure 2-3: Schematics of the analytical link between t_0 (twt), v_0 , and R_{NIP} in case of a homogenous velocity v_0 . Based on the figures from (Thorkildsen, 2019; Javed, 2012)

In a homogenous medium, it is possible to create a link between parameters A and C (Figure 2-3). This subsection is mostly based on previous works of Thorkildsen (2019) and Asgedom et al. (2012b) and gives an overview of the parametric link.

From Equation 2.5, A and C are given as follows,

$$A = \frac{2\sin\alpha}{V_0} \quad C = \frac{2t_0\cos^2\alpha R_{NIP}}{V_0} \quad (2.6)$$

where α is the emergence angle of the central ray that connects the diffractor point to the reference point, m_0 . Moreover, V_0 is the near-surface velocity, and R_{NIP} is the wavefront curvature of the Normal-Incident Point wave measured at the reference point m_0 . In case of a homogeneous velocity model, it follows from Figure 2-3 that R_{NIP} is $1/R = \frac{2}{V_0 t_0}$ (Thorkildsen, 2019).

Use of this latter expression for R_{NIP} , leads to this alternative equation for parameter C,

$$C = \frac{2t_0\cos^2\alpha R_{NIP}}{V_0} = \frac{4\cos^2\alpha}{V_0^2} = \frac{4}{V_0^2} (1 - \sin^2\alpha) \quad (2.7)$$

From Equation 2.6 it follows that $\sin\alpha = \frac{AV_0}{2}$, which can also be combined with Equation 2.7 to give,

$$C = \frac{4}{V_0^2} \left(1 - \left(\frac{AV_0}{2}\right)^2\right) \quad (2.8)$$

The parameter C can be further modified in case of an inhomogeneous model by including the NMO-velocity at the reference point (m_0, t_0),

$$C = \frac{4}{V_{nmo}^2} \left(1 - \left(\frac{AV_0}{2}\right)^2\right) \quad (2.9)$$

In a velocity analysis, the reflected energy is the «controlling» part of V_{NMO} . In the case of dipping structures, apparent velocities should then be used (Levin, 1971). This process requires the NMO-velocity to multiply with the Levin correction factor $\cos\theta$, where θ is the dip. Thus, parameter C with the Levin factor included leads to,

$$C = \frac{4}{V_{nmo}^2(\cos(\theta))} \left(1 - \left(\frac{AV_0}{2}\right)^2\right) \quad (2.10)$$

Since equation 2.10 is dependent on parameter A and the Levin factor, this makes it a two-parameter search. In general, information about the dominating dip in the subsurface is important information. However, in case of a gently dipping overburden, the Levin factor should not be allowed to vary much from 1 to avoid unphysical solutions (Thorkildsen, 2019). Further insight into Equation (2.10) can be obtained by considering the case of a stratigraphic overburden where $\cos\theta = 1$. Combination of Equations 2.7 and 2.10 gives now,

$$C = \frac{4}{V_{nmo}/\cos\alpha} \quad (2.11)$$

In this way, the flanks of the diffractions are easier to detect by the optimal stacking parameters, since the apparent velocity replaces the true velocity (Thorkildsen, 2019).

2.4 Double Square Root equation (DSR)

Due to the Taylor expansion, the CDS operator becomes inaccurate in the case of large apertures in midpoint and offset (Facciopieri et al., 2016). It is therefore necessary to consider small apertures in offset. However, to obtain a good separation of diffractions using CDS, a fairly large aperture in midpoint coordinates is still needed. As an alternative to CDS, the DSR operator has been proposed which is based on the well known Double Square Root traveltime equation (Facciopieri et al., 2016).

As a stacking operator for diffractions, DSR provides an exact traveltime for a point diffractor in a homogenous medium (Thorkildsen, 2019; Facciopieri et al., 2016). It is given by Equation 2.12, where $\Delta s = \Delta m - h$ and $\Delta r = \Delta m + h$. The actual derivation of this equation is given in Appendix A.

$$t_{dsr}^2(\Delta s, \Delta r) = \left[\frac{1}{2} \sqrt{(t_0 + A\Delta s)^2 + C\Delta s^2} + \frac{1}{2} \sqrt{(t_0 + A\Delta r)^2 + C\Delta r^2} \right]^2 \quad (2.12)$$

In the case of stacked data ($h=0$), equation 2.12 simplifies to,

$$t^2(\Delta m, h = 0) = (t_0 + A\Delta m)^2 + C\Delta m^2 \quad (2.13)$$

To obtain optimal values of the stacking parameters A and C, the parametric link in Equation 2.10 is beneficial. Therefore, the derivation of the CDS operator was included in this thesis work to give the proper background to understand Equation 2.10.

Both CDS and DSR operators assume small velocity variations across the stacking surface. However, extensive testing on more complex models demonstrated that the DSR operator is

performing overall better than CDS (Faccipieri et al., 2016). Thus, in this work, the DSR operator has been employed for all data cases.

2.5 Pragmatic search

An effective way to save computational time is to perform a pragmatic search to find the stacking parameters. This process will decrease the data volume but may cause a non-optimal final result (Thorkildsen, 2019). The parameter A in Equation 2.5 describes the moveout as a function of the midpoint coordinate in the zero offset domain. In contrast, parameter C describes the moveout as a function of offset in the CMP domain and also the Δm moveout (Thorkildsen, 2019). Equation 2.14 is the simplified form of Equation 2.5 in the case of the constant midpoint (CMP domain, Δm is equal to 0).

$$t^2(0, h) = t_0^2 + Ch^2 \quad (2.14)$$

which is the conventional NMO-equation as expected. Thus, parameter C can initially be found employing a standard velocity analysis. Setting Equation 2.1 equal to Equation 2.14 gives $C = \frac{4}{v_{nmo}^2}$. Parameter A is found by semblance analysis after stacking (zero-offset domain) (Thorkildsen, 2019). Introducing parameter $h = 0$ in Equation 2.5 gives,

$$t^2(\Delta m, 0) = (t_0 + A\Delta m)^2 + C\Delta m^2 \quad (2.15)$$

where also the analytic link between A and C should be used.

2.6 Coherency measure

During the DSR stacking process, it is essential to select surfaces or curves (hyperbolic curves) that best fit the diffraction traveltimes. It can be challenging to carry out this process when noise is strong. Thus, it is needed to introduce a suitable measure of coherency since the coherent part of the target signal determines the optimal traveltimes curve. In the case of noisy datasets, the most frequently used coherency measure is semblance. It represents the energy of the stacked trace divided by the sum of energy of each individually stacked traces in a time window (Lima et al., 2011). Semblance is defined by the following expression,

$$S = \frac{\sum_{i=k-\frac{N}{2}}^{k+\frac{N}{2}} (\sum_{j=1}^M f_{ji})^2}{M \sum_{i=k-\frac{N}{2}}^{k+\frac{N}{2}} (\sum_{j=1}^M f_{ji}^2)} \quad (2.16)$$

and is a normalized similarity measure between 0 and 1. The inner summation with index j represents the traces in a stacked section, and the outer summation with index i represents the stack of different time samples within a given time window with a half-width of w (width= $2w+1$). The width of the window should relate to the length of the signal wavelet of the event (Lima et al., 2011). However, no emphasis was put on optimizing the time window.

The semblance value close to one implies a perfect coherency. However, in the case of random noise, the semblance value will be approaching zero. The signal to noise ratio can affect the semblance value when in use to find the stacking parameters. To find the stacking parameters for diffraction, will require a significant data volume for the search, which will also lead to increased computational time (Thorkildsen, 2019). The computational time is not the only consequence of the use of semblance. It also has problems in the case of closely interfering events (Asgedom et al., 2012a). The coherency measure is not dependent on the actual amplitude, however, stronger events tend to dominate.

2.7 Post-stack enhancement (combined stacks)

In classical seismic processing, the output is a conventional stacked section. Such a section is assumed to approximate the zero offset (ZO) case. As already discussed, most diffractions are masked by the stronger reflections and not visible in the stack. However, diffractions carry beneficial information about fine-scale structures in the subsurface of significant importance (Kanasewich & Phadke, 1988). A fault is an example of a potential petroleum trap.

To generate more advanced images of the subsurface, we propose in this thesis work to use the following procedure:

- i) Generate a conventional stack
- ii) Generate a diffraction stack based on the DSR approach
- iii) Make a new section by mixing the sections from i) and ii) with a proper scale factor

The next subsection describes briefly post-stack time migration employing the Kirchoff method. It is used in this thesis work to obtain final images of the subsurface based on the various types of input stacks.

2.8 Post-stack time-migration

The purpose of migration is to create a reflectivity map of the area of interest from seismic data recorded at the surface (Gazdag & Sguazzero, 1984). The simplest approach to migration is known as diffraction stacking (also known as diffraction summation migration). The subsurface model is gridded and in each grid point, a potential point scatterer is placed. The corresponding response from such a scatterer is given by the diffraction curve in time. In a constant velocity model, this diffraction curve is given by a simple analytical expression. The case of a stratigraphic earth model can easily be handled by using the NMO-equation. Figure 2-4 shows an illustration of the diffraction stack, where the migrated trace is obtained by summing the input traces along the diffraction hyperbola and place it at the position of its apex.

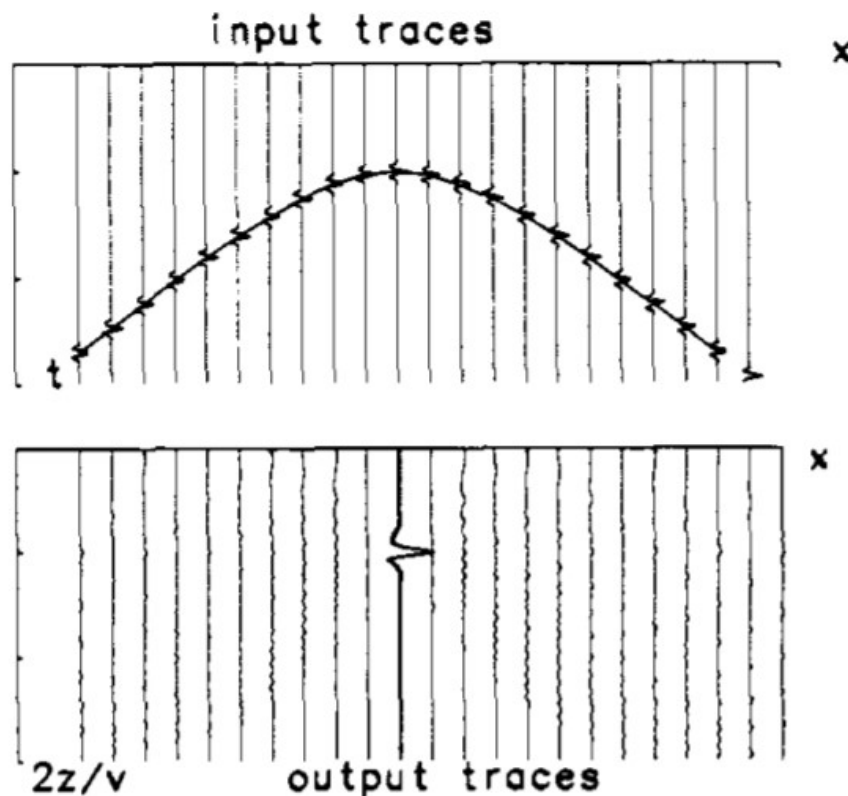


Figure 2-4: Schematics of diffraction summation migration. From (Gazdag & Sguazzero, 1984)

2.8.1 The Kirchhoff migration method

Diffraction-summation migration does not contain any amplitude factors (Gazdag & Sguazzero, 1984). Using wave-theory as a starting point, an improved algorithm can be obtained including amplitude weight factors. Such a migration type is denoted Kirchhoff migration.

In the case of two-dimensional (2-D) seismic, the recorded data can be represented as $p(x, z=0, t)$, where x defines the surface coordinate, z is the depth, and t is the two-way time (Gazdag & Sguazzero, 1984). The migrated image at a depth point (x, z) can be expressed by the equation,

$$p(x, z, t) = \int \frac{\cos(\theta)}{\sqrt{2\pi r c}} \partial_t^{\frac{1}{2}} p(x, z=0, t = \frac{r}{c}) dx \quad (2.17)$$

Equation 2.17 represents an integration along the diffraction hyperbola defined by the traveltime curve $t=r/c$ with $r=\sqrt{x^2+z^2}$ (constant velocity case). This equation is similar to the diffraction summation method because of the integration, but now contains a weight-factor and the factor $\partial_t^{\frac{1}{2}}$ representing the half derivative with respect to time t .

By introducing the NMO-velocity in Equation 2.17 the case of a stratigraphic model can be handled. Since the NMO-velocity is given in time, the output from migration will then be a time-migrated image.

3 Workflows, apertures, and search parameters

3.1 Diffraction stacking - workflow

Diffraction separation is carried out employing the DSR operator, and stacking along the diffraction surface in midpoint and offset (Thorkildsen, 2019). The stacking operator will determine the travel time of diffraction using the parameters A and C. To obtain optimal parameters, several tests need to be run with varying apertures in offset and midpoint. The output from this workflow will be a diffraction-enhanced stack. Besides, the conventional stack is also computed. These two types of stacks can be combined with proper weighting applied, to give more a more balanced stack between reflections and diffractions. In the case of each type of stack, a final image can be obtained employing post-stack time-migration (Kirchhoff type).

Figure 3-1 shows the detailed workflow for diffraction separation and imaging employed in this thesis work. At the pre-processing step, input data can be either controlled data or field data. In the case of controlled data, two different approaches were used here. The first one was to apply the NUCLEUS+ software from PGS to generate finite-difference data. Alternatively, input data could be controlled data taken from the literature (SIGSBEE 2A used in this thesis work). After CMP sorting of the input data, the next step is to determine an initial model for the C parameter. In the case of non-complex synthetic data, parameter C was obtained from a simplified automatic velocity analysis using Matlab code. In the case of more complex controlled data or field data, the initial C parameter could be determined from a velocity analysis using the commercial software package ProMax. This approach will minimize the effect of possible multiples present in the data (Thorkildsen, 2019). In the examples presented in this work, the C parameter was determined using the Matlab program. In the case of the complex SIGSBEE 2A model, a depth velocity model was supplied. This velocity model was then converted from interval velocities in-depth to stacking velocities in time using Promax. After proper stacking, parameter A can be obtained from the semblance analysis, where the search for this parameter is in the midpoint domain. In practice, this is a two-parametric search employing the parametric link between A and C (Thorkildsen, 2019). A final optimization is applied before generating the diffraction stack using coherency thresholding. This stack can also be Kirchhoff time-migrated using software from the CREWES consortium.

There are several ways to obtain optimal stacking parameters. The pragmatic search has been chosen for this work because the computational efficiency makes it more attractive. To increase the accuracy of the pragmatic search, multi-domain refining was employed (Thorkildsen, 2019). The multi-domain search will scan over small changes in parameters and represents final minor adjustments. The input parameters are allowed to vary with small ranges given in percentage and will not change much in the final search. The coherency map can be applied to threshold the final output stack. The use of the coherency map obtained during the midpoint search gives the most useful results. The stack obtained after the use of proper coherency thresholding consists mainly of diffracted energy (Thorkildsen, 2019).

In this thesis work, we will employ two different versions of coherency thresholding. The first approach is to multiply the diffraction-enhanced stack with the coherency map. When used, the result is labeled with «Endrias», to give credit to the earlier work of Asgedom et al. (2011). The second approach is to use the semblance plot to remove parts of the diffraction stack that falls below a user-defined threshold. When used, the result is labeled «Vemund», to give credit to the earlier work of Thorkildsen (2019).

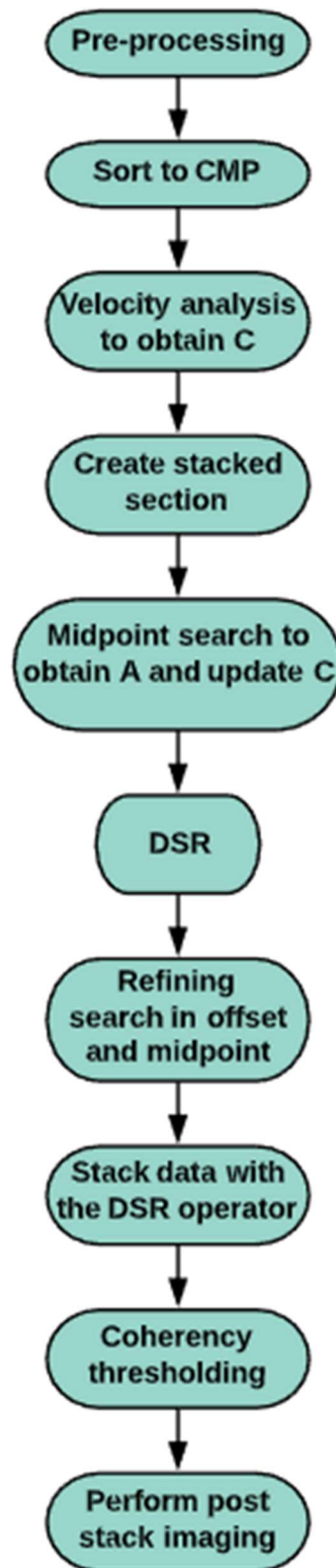


Figure 3-1: workflow for diffraction-stacking and imaging. Based on (Thorkildsen, 2019)

3.2 Apertures (δ) – general observations

The size of the apertures has a considerable impact on stacking quality (Facciopieri et al., 2016). One needs to set a limit on how many neighboring CMPs to consider, thus how far the midpoint displacement should be. In Facciopieri et al. (2016) an analytical expression for the aperture in the midpoint, $\delta^{(m)}$ is introduced based on Fresnel zone estimates. Moreover, the aperture in offset is proposed to be the same as the one used in conventional CMP-stacking:

$$\delta_{Diffraction}^{(m)} = \delta_{Diffraction}^{(h)} = \delta_{CMP}^{(h)} \quad (3.1)$$

where δ is the aperture and h is the half offset.

From extensive testing, as reported in Facciopieri et al. (2016), a good diffraction separation is obtained when the aperture in midpoint is chosen (much) larger than the corresponding aperture in offset. The choice of a small aperture in midpoint will not separate diffractions well and will give an output stack dominated by reflections.

3.3 Choice of search parameters

The pragmatic search for the parameters A and C is based on the link described by Equation 2.10. This equation is jointly applied with Equation 2.4 because of the angle α . This angle can range from -90° to $+90^\circ$, thus a theoretical range for parameter A of $\pm \frac{2}{v_0}$. This full range is not necessary because, in practice, the diffractions associates with such large emergence angles are negligible (Thorkildsen, 2019).

The search range for the multi-domain refinement is given as a perturbation in the percentage of the existing A and C parameter values. To ensure computational efficiency, the parameter perturbation during the refinement stage should not be too large. If the parameters are allowed to vary significantly from the initial values, this may lead to other local maxima in semblance that does not represent any form of coherency with the diffractions (Thorkildsen, 2019).

4 Software demonstration using controlled data

As already briefly discussed, several software packages and Matlab codes have been employed in this thesis work:

- NUCLEUS + (PGS) has been used to generate controlled finite-difference data.
- ProMax has been used to convert velocities from depth to time and also to quality control velocity analyses. Besides, the package has been employed to generate high-quality images.
- Matlab code: has been used to determine parameters A and C using the pragmatic search, and generate as output both conventional stacks as well as diffraction-enhanced stack based on the DSR operator.
- CREWES code: employed to do post-stack time-migration of the various types of the stack.

In the next subsections, a demonstration of the use of the various software packages and codes is presented using a controlled data set.

4.1 Generating controlled data using Nucleus+

Nucleus+ is a Survey Modelling module developed by Petroleum Geo-Services (PGS). Among others, it contains a finite-difference modeling tool that was used to perform 2D modeling in this thesis work.

The diagram in Figure 4-1 shows the essential inputs to complete a 2D finite-difference modeling. It follows from this figure that three main steps are needed: (i) create a velocity model, (ii) a grid survey, and (iii) a shooting vessel.

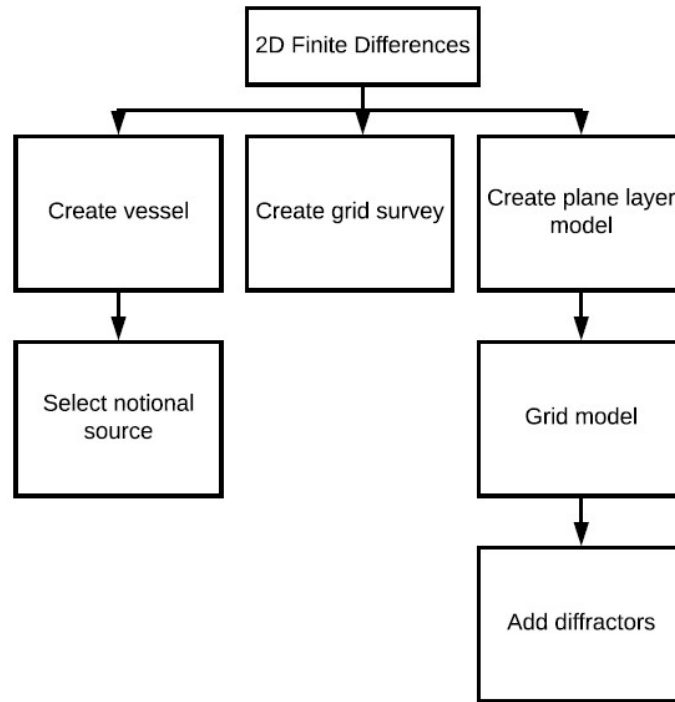


Figure 4-1: Flow chart of the main steps in FD-modelling in NUCLEUS+

Starting with the source vessel, it defines the source and receiver positions as well as the sample interval and recording length (Nucleus-Help, 2020). As a part of creating a vessel, it is necessary to select the single notional source signature dataset that connects the seismic source of the vessel. Figure 4-2 shows a plot of a source vessel set up in 3D with six streamers and flip-flop sources.

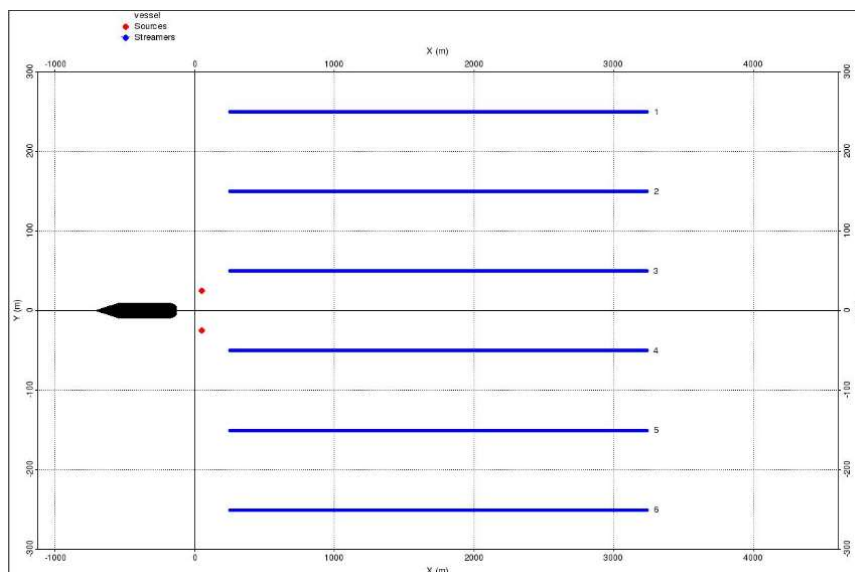


Figure 4-2: Example of a vessel plot in 3D. The blue lines are the six streamers, and the two red dots represent the sources.

In the controlled data example employed here, a 2D survey was employed.

The grid survey defines the coordinates of the model. The receiver positions are given relative to the shot point. In a case of a regular grid for both shots and receivers, it is only necessary to specify the coordinates of the first shot. It is also required to define the shot increment and the distance between the flip-flop sources if 3D (Nucleus-Help, 2020). Figure 4-3 shows a plot of a 2D source vessel superimposed in the model grid.

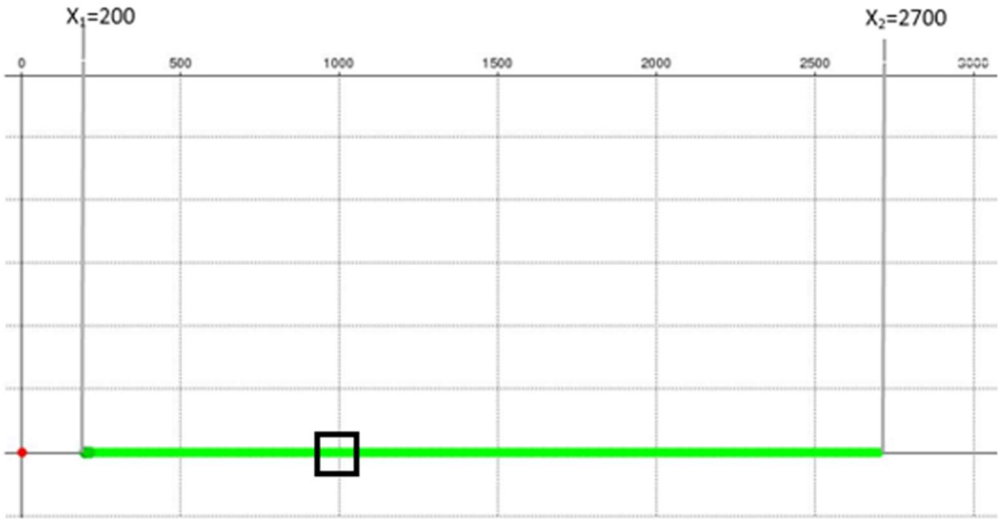


Figure 4-3: a 2D survey with the minimum(x_1) and maximum(x_2) offset. The red dot indicates the source and the green part, the receivers.

A summary of the parameters chosen for the 2D survey used in this work is summarized in Table 4-1. In the simulations, a sample interval of 2 msec and a center frequency of 40 Hz was selected.

Number of shots	401
Shot interval	25m
Number of groups	240
Group interval	12.5m
Min offset	200m
Max offset	2700m

Table 4-1: Survey design parameters

The final step in preparing for the FD-modelling is to define the model itself.

A plane layer model in Nucleus may consist of plane dipping layers and diffraction points. The plane interface can dip in all directions, but the interfaces cannot intersect inside the model area

(Nucleus-Help, 2020). The layer parameters are in the case of a full elastic model: P-wave and S-wave velocities, densities, and P-wave and S-wave Q factors (Nucleus-Help, 2020).

The model employed here consisted of a dipping layer and a point scatterer placed in the lower layer. Figure 4-4 shows its geometry and with assigned P-wave velocity. Synthetic data were generated for the acoustic case only.

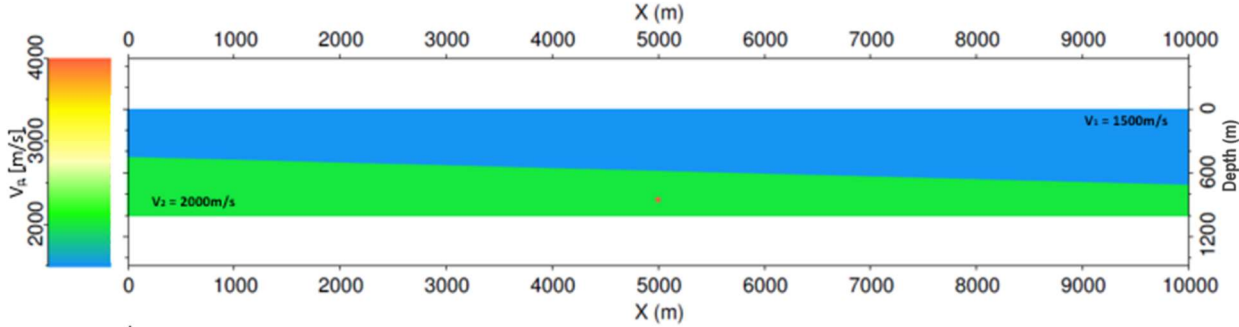


Figure 4-4: P-wave velocity model.

From Figure 4-4 it follows that the upper layer is the water layer with a velocity of 1500m/s, and the lower layer has a sediment velocity of 2000m/s. The diffraction point is positioned approximately in the middle (5000m) of the model and in the lower layer. Figure 4-5 a) shows a depth slice (850m) through this point scatterer. The diffractor has a contrast of 100% (strength factor) relative to the velocity of the embedded layer and a radius of 25m. Thus, the scatterer is strong. Figure 4-5 b) shows a zoomed-in version of the scatterer showing that it is well defined. The small step-like pattern around its edge is expected due to the use of a finite-difference formulation (i.e gridded model).

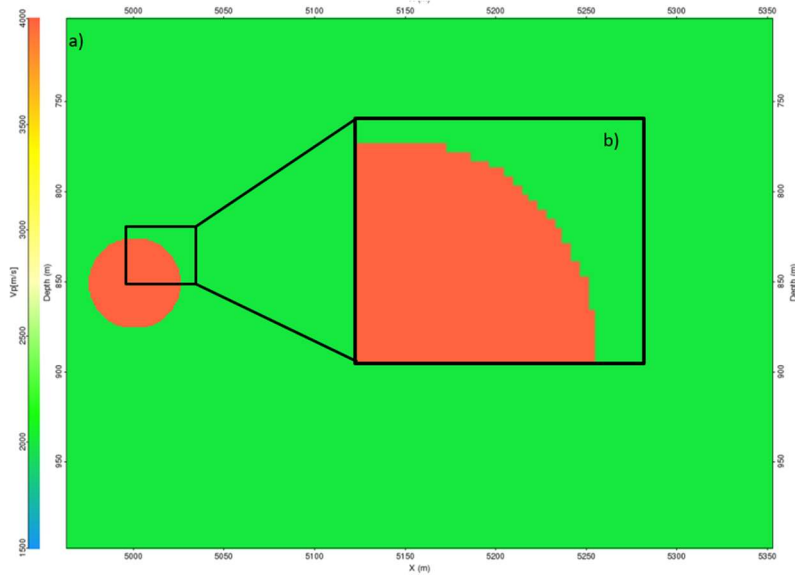


Figure 4-5: a) the strong diffractor at $x=5000\text{m}$ and 850m depth b) zoomed-in version of the scatterer showing the step-like pattern.

Figure 4-6 a) shows one shot point gather output from the FD-modelling. In this subfigure, all events are present including the strong direct wave. After the removal of this latter wave, the result that is shown in Figure 4-6 b) was obtained and could be input to the diffraction-enhancement software.

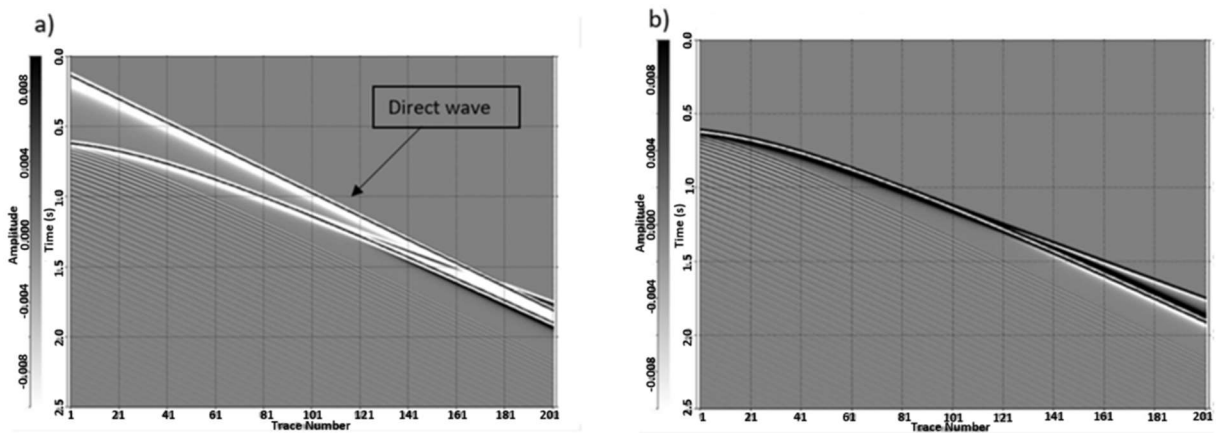


Figure 4-6: a) Example of source gathers output from finite-difference modeling with direct wave. b) The same source gathers after removal of direct wave.

A well-known problem in FD-modelling are artifacts caused by gridding. The grid size has to be small enough to ensure stability and as little numerical dispersion as possible. However, the grid size can not be chosen too small since it will lead to a significant increase in computational time.

4.2 Diffraction-enhancement using MATLAB code

The Matlab code employed in this thesis work has been developed by Thorkildsen (2019). It represents an implementation of the DSR approach to diffraction enhancement and stacking. As explained earlier, first the parameter C was obtained through a standard automatic semblance-based velocity analysis, followed by a joint parametric search of A linked with C. A refinement of the model parameters was then included, before the final diffraction-enhanced stack was output after proper thresholding.

A sparse number of events and a majority of zero time-sample values characterized the synthetic data generated. To condition the data to better fit with real data, white-noise was added to each trace (25%). Figure 4-7 shows a selection of source gathers after white-noise addition.

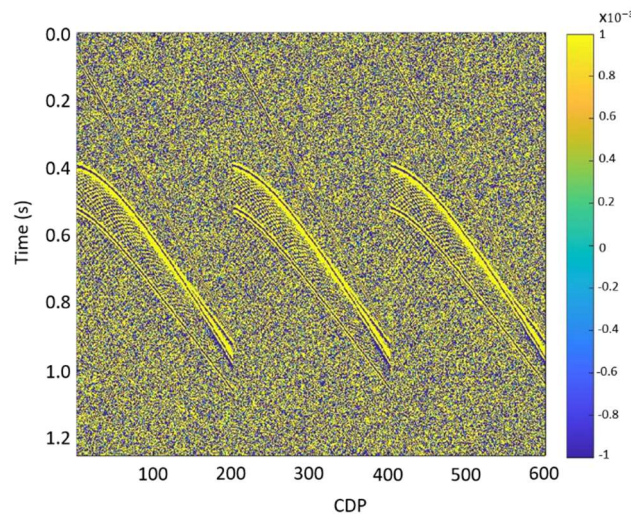


Figure 4-7: A selection of source gathers after white-noise addition.

Based on input data as shown in Figure 4-7, the actual diffraction-enhancement was carried out following the steps outlined before. In the first step, the parameter C was determined from a conventional semblance-based velocity analysis. The optimal choice of the half-offset aperture was found to be 500m.

In Figure 4-8 the optimal stacking or NMO-velocity field is shown based on the semblance criterion. As soon as the velocities have been determined they can easily be transformed to the parameter C using the relationship $C = \frac{4}{V_{nmo}^2}$. From Figure 4-8 (left) it can be seen that the stacking velocity associated with the dipping layer is close to that of water as expected. Regarding the scatterer, the diffraction curve is characterized by increasing velocities along the flanks due to the increasing apparent dip. Due to the white-noise addition, artificial velocity

values are present both above the dipping layer and elsewhere. However, based on the semblance plot shown in Figure 4-8 (right), only the true dipping event and the diffraction are characterized by high semblance values.

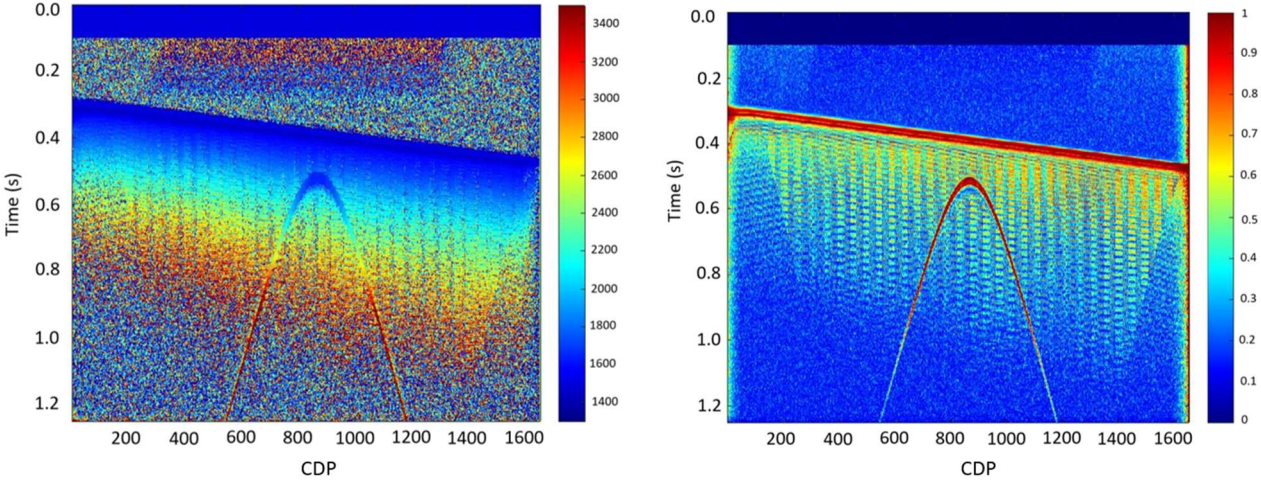


Figure 4-8: Left: The optimal velocity field output from semblance analysis and right: corresponding semblance panel.

Having determined the NMO-velocity field, a conventional stack of the data can be obtained as shown in Figure 4-9. This stack is then inputted to the next step, which purpose is to determine the parameter A based on a semblance search in the midpoint direction. To make this search more robust the link between the A and C parameters is being employed and the C parameter is also updated. For this particular data set, an aperture of 1200m in midpoint was found to work well. Two other choices of aperture (800m and 1000m) were also tested but with a poorer result.

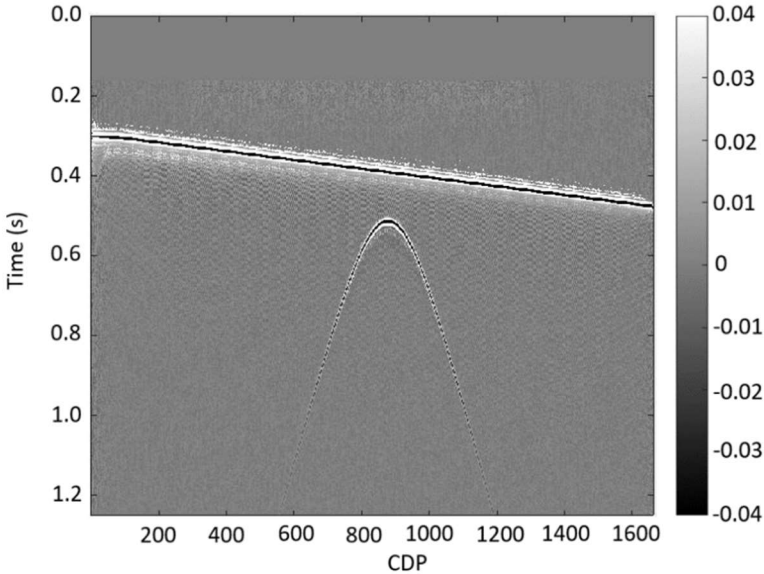


Figure 4-9: conventional NMO stack.

Figure 4-10 shows a plot of the A parameter determined from the semblance analysis in the midpoint-domain. Since this parameter is closely connected with the take-off angle of the central ray and also with the dip angle for a simple model, it is as expected that A is constant along with the dipping event and changes sign from one flank to the other of the diffraction curve. Due to the joint A and C analysis through the analytical link, also the C parameter is slightly updated at this stage (cf. Figure 4-10 to the right)). The semblance panel associated with the midpoint search is shown in Figure 4-11. The semblance value is seen to be highest at the apex of the diffraction curve and degrade with steeper flanks.

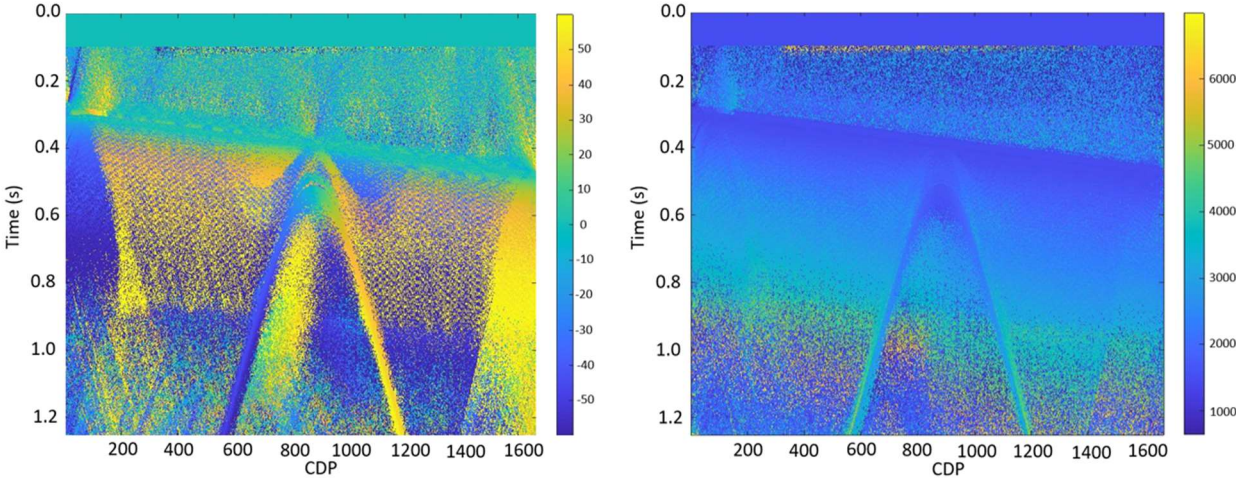


Figure 4-10: Plot of A parameter (left) and updated C parameter (right) for aperture Δm 1200 and Δh 500.

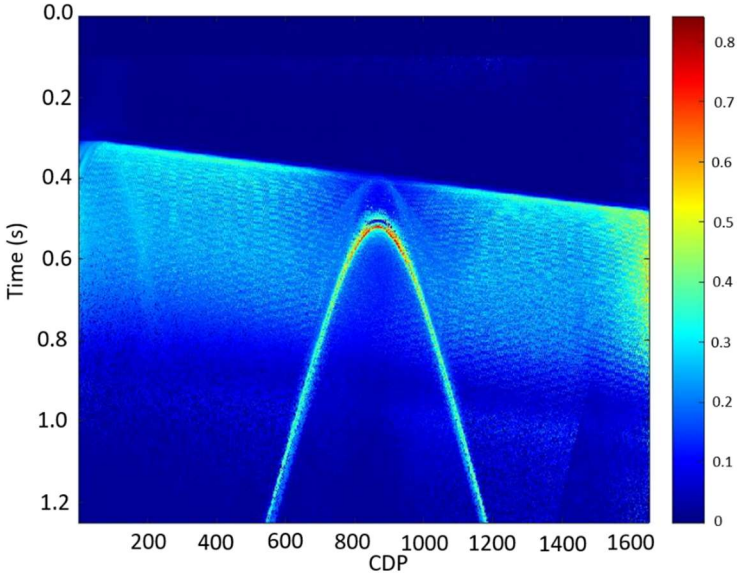


Figure 4-11: Semblance panel output from midpoint search for an aperture of Δm 1200 and Δh 500.

Before generating the diffraction-enhanced stack, a multi-domain (both offset and midpoint) refinement step is included. During this refinement, only smaller adjustments of parameters A and C are allowed. The corresponding updated versions of Figure 4-10 and Figure 4-11 are now given in Figure 4-12 and Figure 4-13.

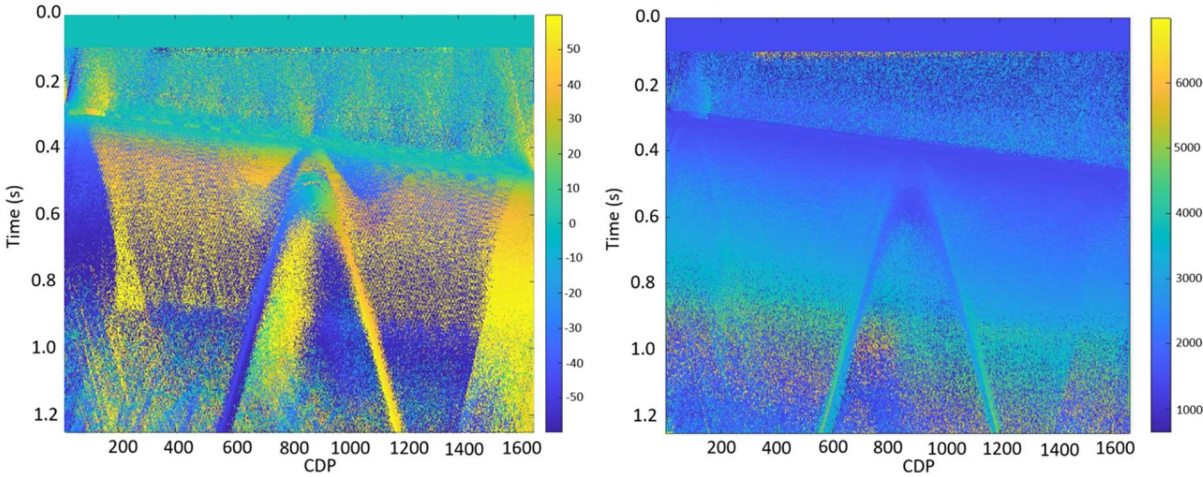


Figure 4-12: Plot of parameter A (left) and C(right) after multi-domain refinement for aperture Δm 1200 and Δh 500.

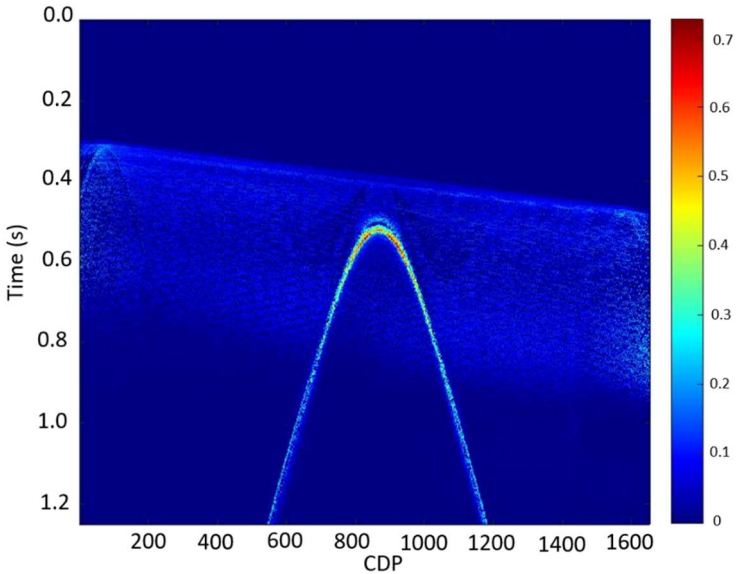


Figure 4-13: The semblance panel after the multi-domain refinement for aperture Δm 1200 and Δh 500.

After the refinement stage has been completed, a diffraction-enhanced stack can be computed using the DSR operator.

The DSR stack before the application of thresholding is shown in Figure 4-14. Traces of the reflection event is still visible and with some additional noise also present. As briefly discussed before, two different approaches to thresholding can be applied. Based on the semblance panel a threshold value is defined by the user, and all values in the corresponding diffraction-

enhanced stack are zeroed. In this thesis work, this approach is labeled «Vemund». The corresponding results are shown in Figure 4-15 employing a threshold value of 0.43. The alternative approach to thresholding is to multiply the diffraction-enhanced stack with the semblance panel. In this work, such a strategy is labeled «Endrias», and the result is shown in Figure 4-16. Direct comparison between Figure 4-15 and Figure 4-16 show that thresholding has worked well in both cases leading to an improved diffraction-enhanced stack. The result in Figure 4-15 is somewhat cleaner but on the other hand, the flanks of the diffraction curve are slightly better enhanced in Figure 4-16.

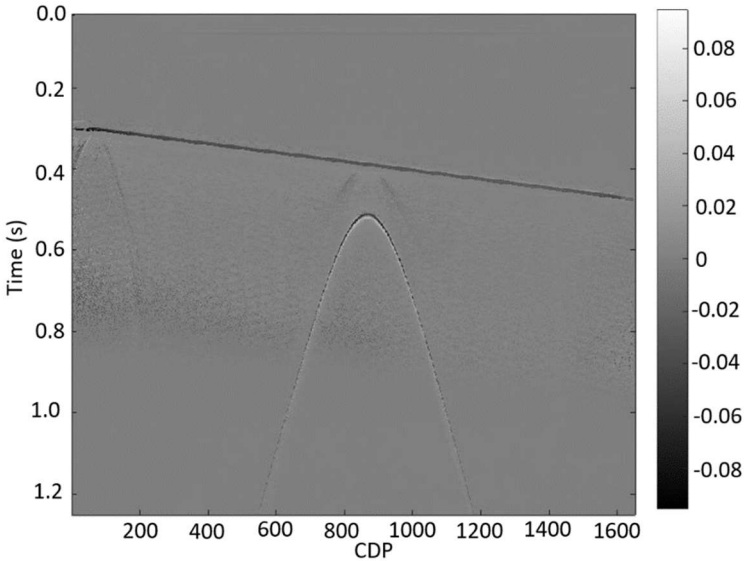


Figure 4-14: DSR stack before thresholding for aperture Δm 1200 and Δh 500.

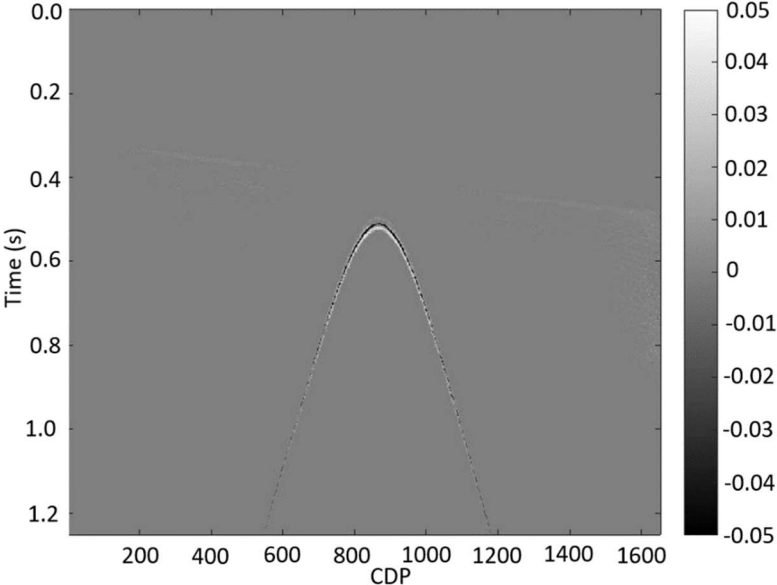


Figure 4-15: DSR stack after thresholding (Vemund) for apertures Δm 1200 and Δh 500.

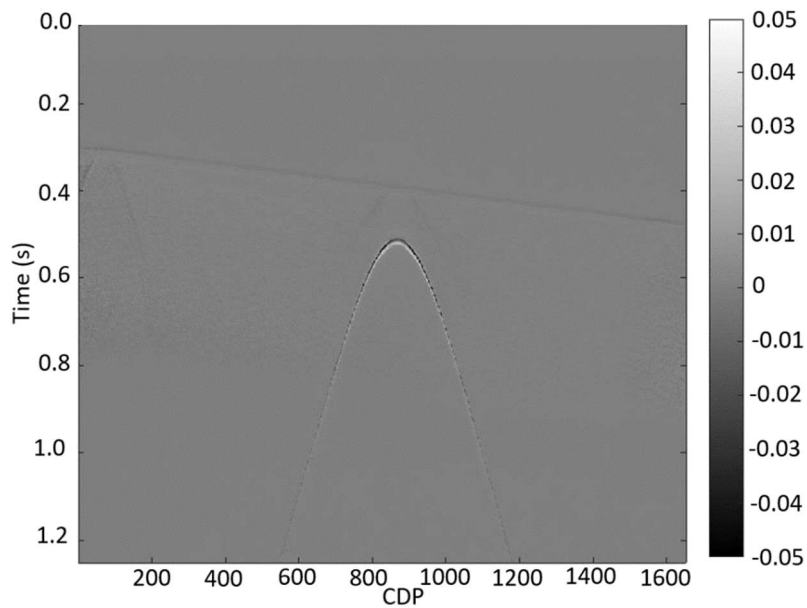


Figure 4-16: DSR stack after thresholding (Endrias) for apertures Δm 1200 and Δh 500.

4.3 Post-stack time-migration using code from CREWES

Post-stack time-migration was carried out employing a Kirchhoff type of code developed by the CREWES consortium. It is part of the CREWES Matlab Toolbox and is created by Xinxiang Li and modified by Dr. G. F. Margrave (Margrave, 2020).

The migration aperture is the key parameter when it comes to Kirchhoff migration. The smaller aperture, the faster computation, but a too-small choice of the aperture will not migrate properly dipping events and especially the deeper ones. In the example discussed here, three different migration (half-)apertures were tested: 500m, 2500m, and 5000m.

It is also necessary to define a value for the migration taper and the maximum dip angle. The migration code of CREWES had a cosine taper. It prevents migration artifacts (controlling noise) by scaling down the amplitudes at the edge of the survey. The maximum dip angle was chosen to be 60 degrees. No anti-aliasing filter was employed to constrain the operator.

Table 4-2 summarizes the choice of migration parameters for the three different cases investigated. Figure 4-17 to Figure 4-19 shows the corresponding migrated results obtained with the diffraction-enhanced stack as input. The diffraction curve is well focused in all three cases, but with less noise present when increasing the aperture. This is especially noticeable in the two areas marked with the blue rectangles and the red rectangles around the diffraction.

Migration aperture (MA)	500	2500	5000
Width of aperture taper (MA x 0.05)	25	125	250
Maximum dip limit (MDL)	60	60	60
Width of angle limit taper (MDL x 0.15)	9	9	9

Table 4-2: choice of migration parameters.

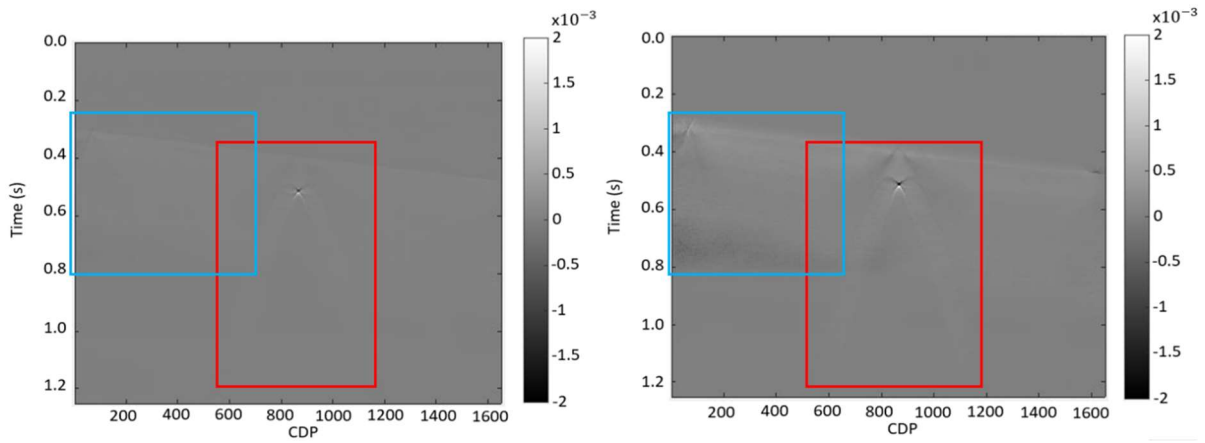


Figure 4-17: image obtained with a migration apertures of 500m. Left: «Endrias» thresholding and right: «Vemund» thresholding of input.

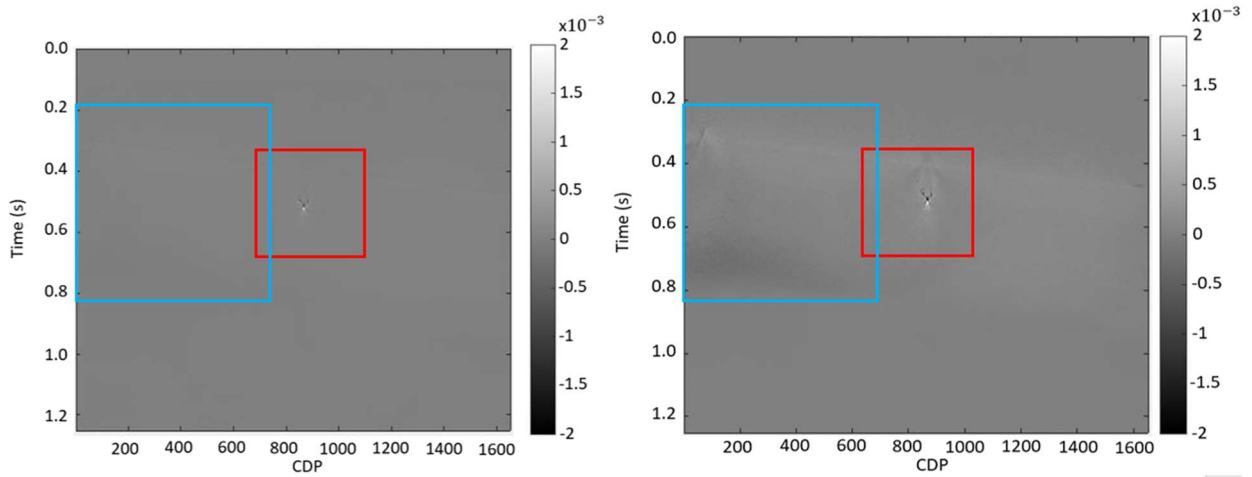


Figure 4-18: image obtained with a migration aperture of 2500m. Left: «Endrias» thresholding and right: «Vemund» thresholding of input.

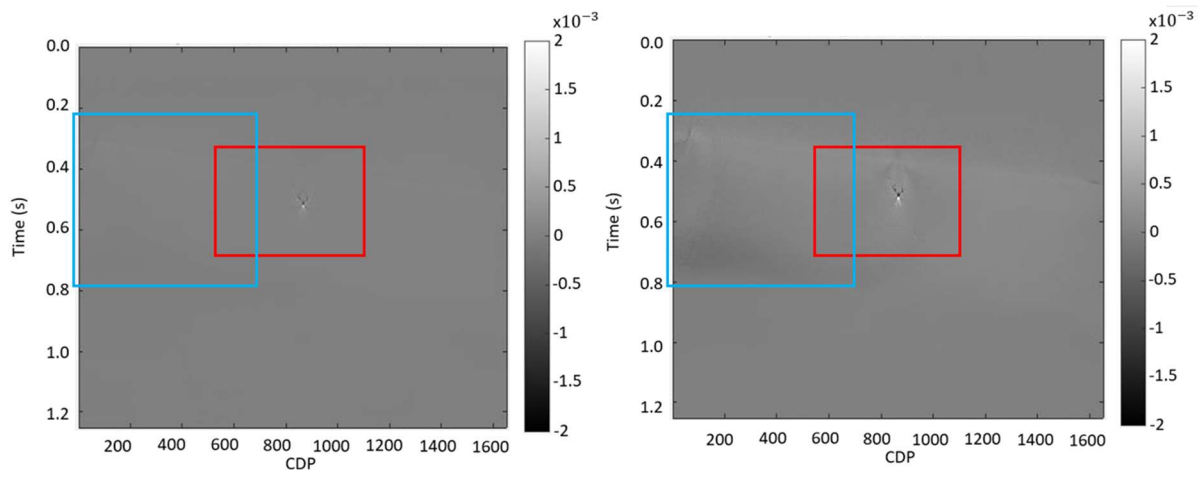


Figure 4-19: image obtained with a migration aperture of 5000m. Left: «Endrias» thresholding and right: «Vemund» thresholding of input.

5 Diffraction separation results – controlled-data studies

In this chapter, two different controlled-data cases are employed to demonstrate and analyze the performance of the DSR approach to diffraction-separation. The first case involves a fairly simple model of two sets of diffraction points embedded in a layered model. This data study serves as a test of the resolution capability of the separation process. The second case is a controlled-data set taken from the open literature: SIGSBEE 2A. It represents a complex and realistic model case including a salt body.

5.1 Simple point-scatterer model

5.1.1 Definition of model parameters

The model consists of five horizontal layers with velocities varying from 4000m/s to 4800m/s (top to bottom). A total of twelve diffraction points are embedded in this model. Four of the scatterers are placed in layer two and the remaining eight are located in layer three. All diffraction points are fairly weak with a contrast of 10% relative to the surrounding medium. Figure 5-1 a) shows a plot of the full model and a zoomed version of the scatterers is given in Figure 5-1 b).

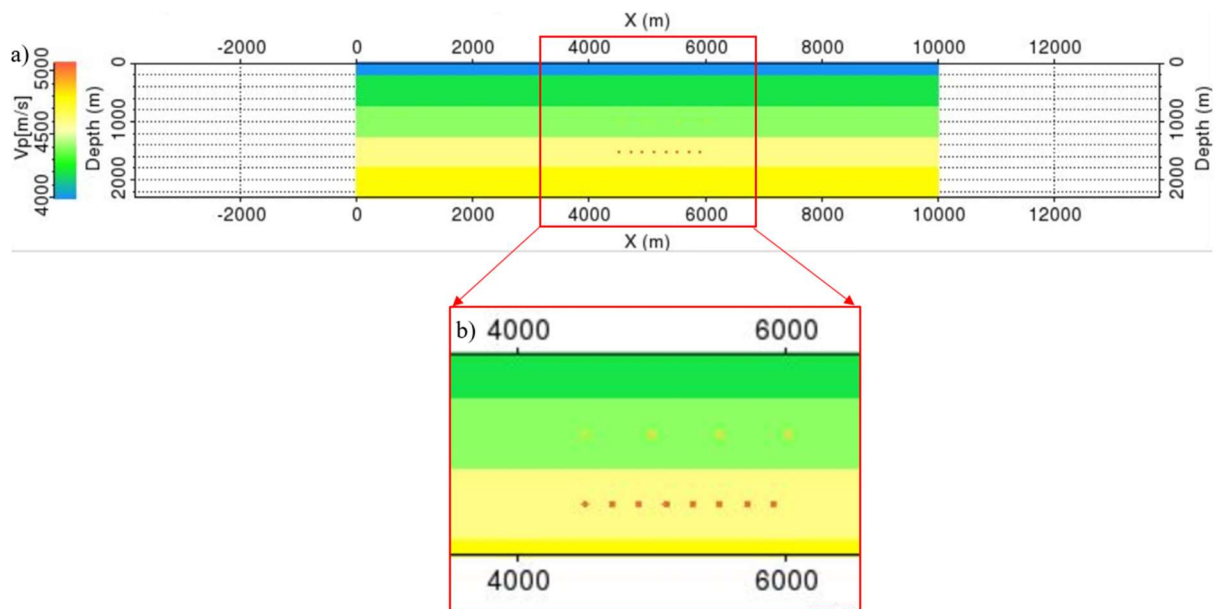


Figure 5-1: a) Overall model (velocity color-coded) and b) zoomed version of the diffraction points.

As always in finite-difference modeling, the choice of grid size is a controlling factor. A small grid size will minimize numerical dispersion but lead to a larger computational burden. Thus,

we need to choose a grid size that represents a good balance between these two issues. In the current study, the grid size was set to 2m and a total record length of 2000ms was chosen. Figure 5-2 shows a plot of a source gathers obtained from this parametrization. The overall quality of the data seems fine.

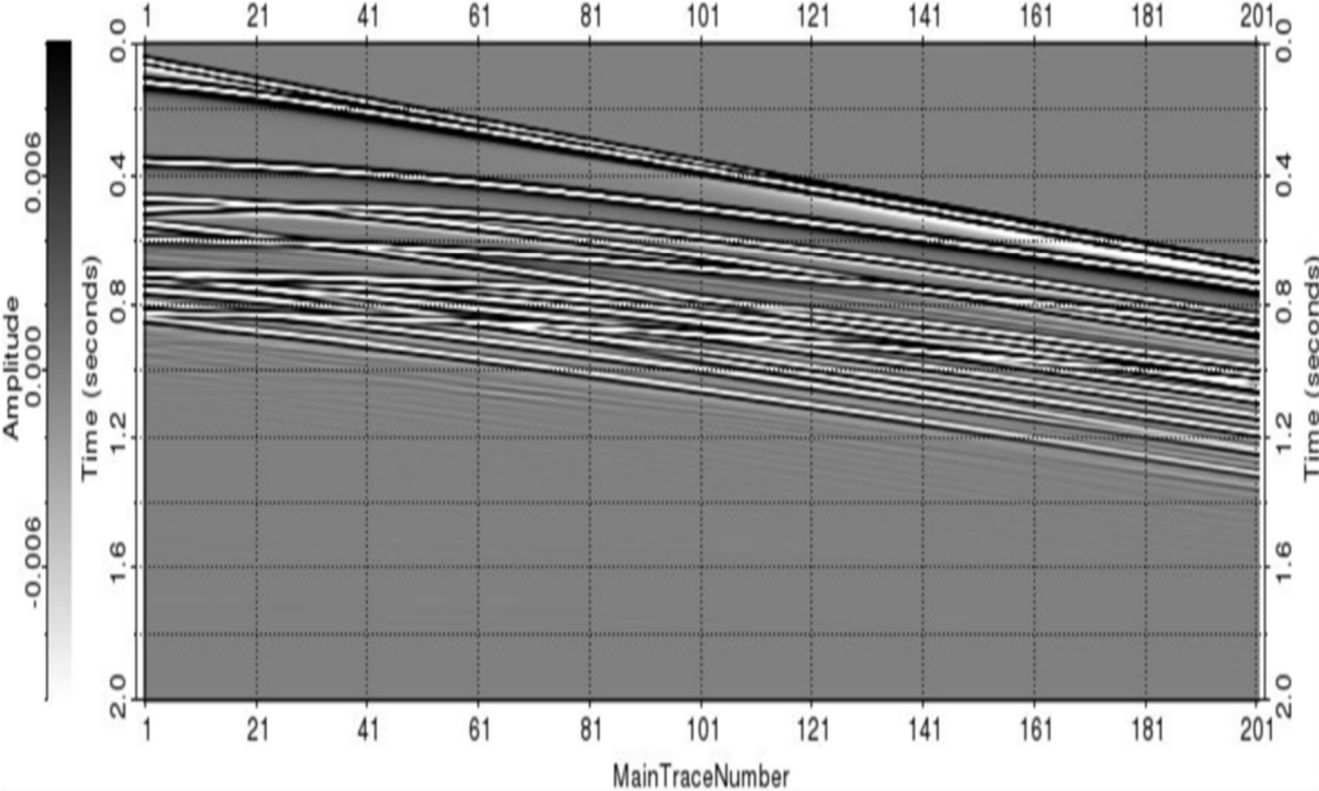


Figure 5-2: Example of a source gather output from FD-modelling.

5.1.2 Basic steps in diffraction-enhancement

Based on the data from the controlled model in Figure 5-1, diffraction-enhancement is carried out. Initially, optimal apertures in mid-point and offset have to be determined. From earlier experience, an aperture of offset of 500m seemed to be a good choice. However, the aperture in mid-point needs to be carefully determined, since it plays a more important role in discriminating between reflections and diffractions. After careful testing, an aperture in midpoint (Δm) of 1500m was found optimal. Two other cases tested, with an aperture of respectively 1000m and 1200m, can be found in Appendix B.

Velocity analysis and NMO stack

A semblance-based velocity analysis was carried out and the result is shown in Figure 5-3 (left). As expected, the velocities will increase along the flanks of the diffraction curves due to the effect of apparent velocity discussed earlier. The highest (apparent) velocity seems to be about

14000m/s and with the apex of the diffraction curves corresponding to a velocity of about 4000m/s as expected.

In the right part of Figure 5-3, the corresponding semblance plot is shown. The semblance peaks at each reflection interface and along the apex of each diffraction curve, and decreases along the flanks of each diffraction.

Based on the velocity model in Figure 5-3, a conventional NMO stack was formed as shown in Figure 5-4. The reflections are strongest, but also the weaker diffractions are fairly visible.

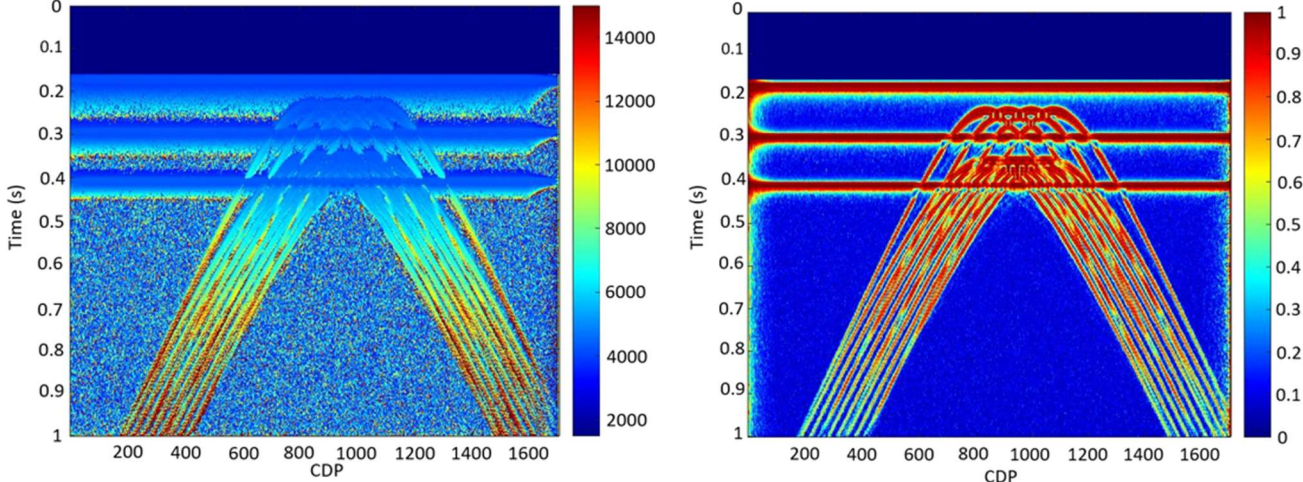


Figure 5-3: Velocity model (left) and the corresponding semblance plot (right)

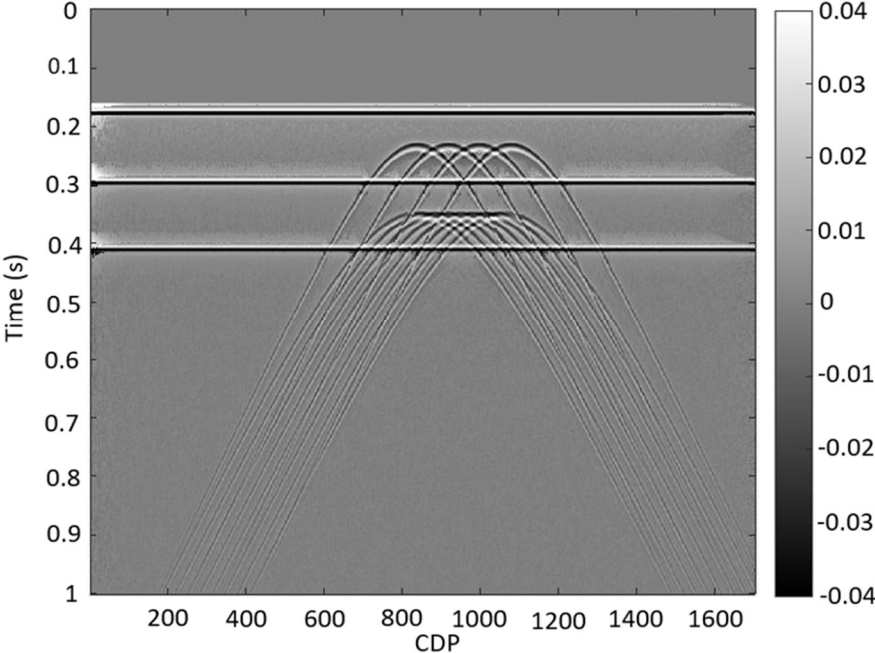


Figure 5-4: NMO stack

Midpoint search

As already mentioned, several tests were carried out to determine an optimal aperture of the midpoint. The best choice was found to be 1500m (for other choices the reader is referred to Appendix B). In these studies, the analytical link between parameters A and C was employed to ease the convergence. The corresponding A (left) and C (right) parameter panels are shown in Figure 5-5. Since the A parameter is directly related to the take-off angle and therefore also relates to the dipping angle, the left and right flanks of each diffraction have opposite signs.

Figure 5-6 shows the corresponding semblance in mid-point. The semblance is seen to be quite good for each diffraction, but with some residual high semblance values associated with the reflections at the boundaries.

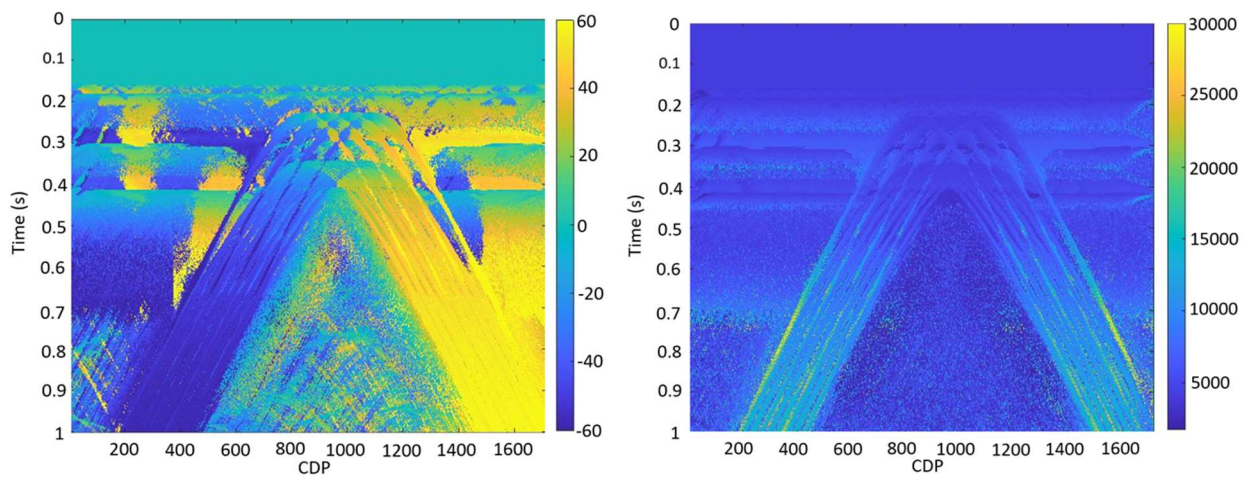


Figure 5-5: A parameter panel (left) and C parameter panel (right) for apertures Δm 1500 and Δh 500

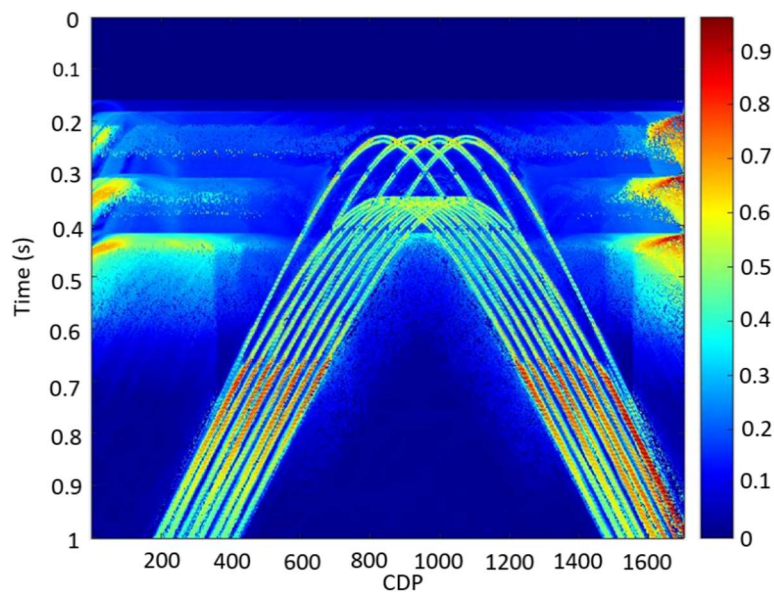


Figure 5-6: Semblance in the midpoint

Refining search

After the A and C search has been completed, a multi-domain refinement search is carried out. During this computation, the parameters A and C are allowed to vary within a rather limited range set in %.

The plot of the semblance panel in midpoint after this refinement is shown in Figure 5-7. Direct comparison with Figure 5-6 shows a cleaner panel after refinement with fewer reflection artifacts.

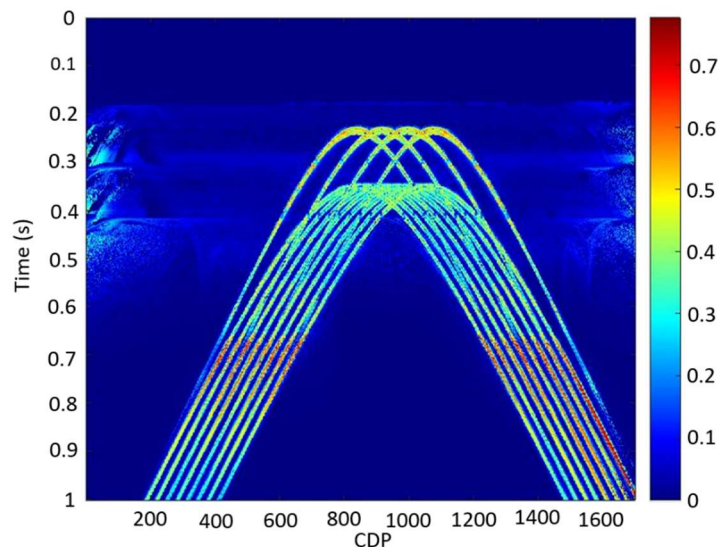


Figure 5-7: Semblance in midpoint after multi-domain refinement

Diffraction-enhanced stack based on DSR (before and after semblance thresholding)

The final step is to form the diffraction-enhanced stack based on the DSR-operator equation and with the use of the optimal A and C parameters determined from the semblance analysis. The brute force diffraction-stack is shown in Figure 5-8. From this figure, contributions from reflections are still visible. Thus, semblance thresholding is needed to obtain a cleaner result.

Figure 5-9 shows the results obtained after thresholding. Two different thresholding strategies have been employed in this thesis work. The difference is that the one denoted «Endrias» implies a multiplication between the brute-force diffraction-stack and the semblance panel. The second approach denoted «Vemund», involves a user-defined threshold, where data in the brute-force diffraction stack are removed in case the corresponding semblance panel value is below the threshold. In the case of the «Vemund» option (left in Figure 5-9), the threshold value was set to 0.43. It can be seen from Figure 5-9 that the diffraction-separation has worked well

in both cases. The «Endrias» option (right in Figure 5-9) gives slightly stronger diffractions but with some more reflection artifacts than the «Vemund» approach.

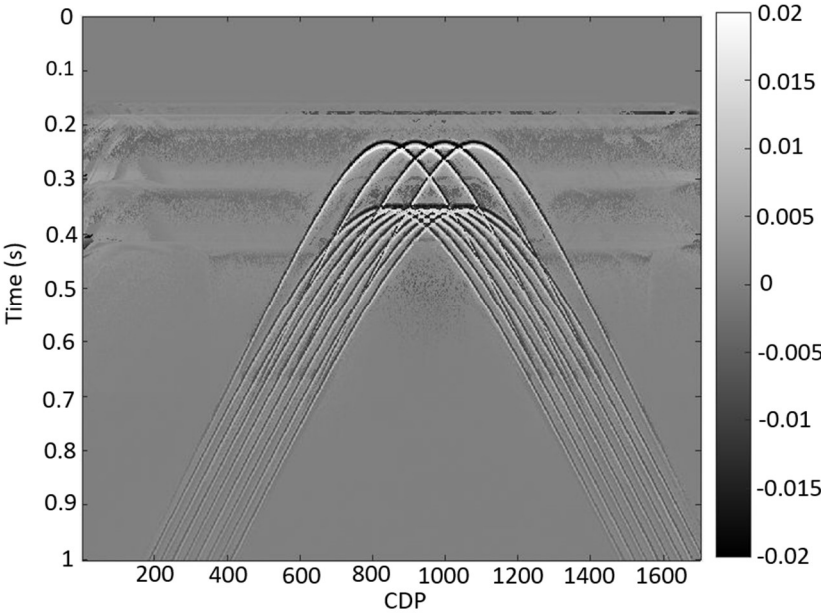


Figure 5-8: Brute-force diffraction-enhanced stack for apertures Δm 1500 and Δh 500

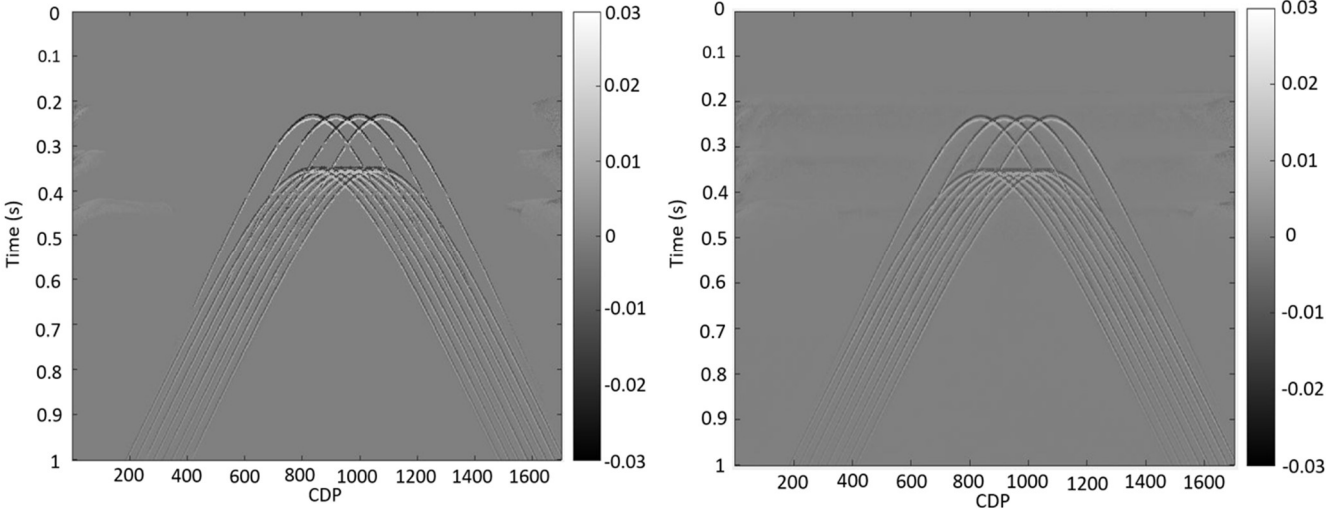


Figure 5-9: Diffraction stack after thresholding. «Vemund» option (left) and «Endrias» option (right)

5.1.3 Combined stacks

Based on the workflow defined in this thesis work, seismic input data can be unconventionally processed to obtain both an NMO-stack as well as a diffraction-enhanced stack.

In many cases, the diffractions will appear weaker than the reflections, and may also be completely masked by the stronger reflections before enhancement. One possibility to generate

a more balanced stack is to form a weighted sum of the NMO- and diffraction-stack (Equation 5.1).

$$Data_{comb} = (1 - \alpha)Data_{NMO} + \alpha Data_{diff} \quad 0 < \alpha < 1 \quad (5.1)$$

Thus, a choice of $\alpha = 0$ gives a classical NMO-stack as shown in Figure 5-10 for the two thresholding options. Moreover, the cases corresponding to respectively $\alpha = 0.3$ and $\alpha = 0.8$ are shown in Figure 5-11 and Figure 5-12. The latter choice of $\alpha = 0.8$ seems to represent a good balance between reflections and diffractions with respect to magnitudes.

For all cases, slight differences exist between the two thresholding options, but neither of these options is better than the other.

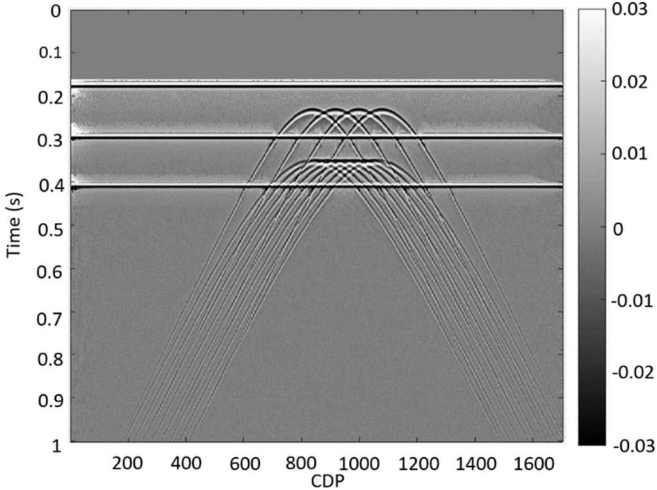


Figure 5-10: NMO-stack ($\alpha = 0$)

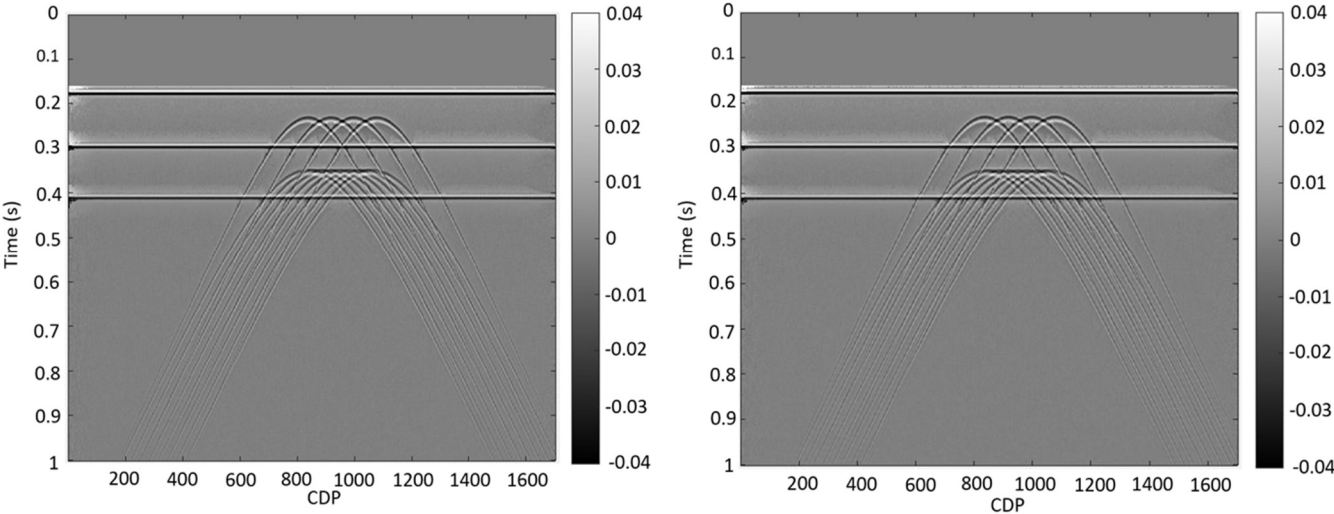


Figure 5-11: Combined stacks corresponding to $\alpha = 0.3$. «Vemund» option (left) and «Endrias» option (right)

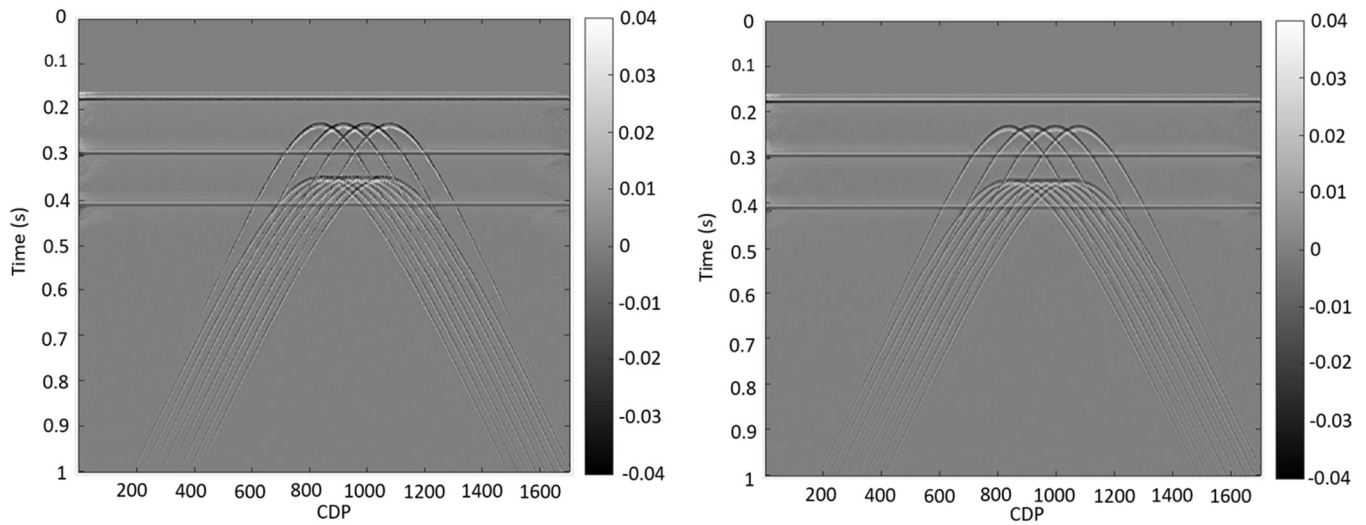


Figure 5-12: Combined stacks corresponding to $\alpha = 0.8$. «Vemund» option (left) and «Endrias» option (right)

5.1.4 Post – stack migration

NMO- and diffraction-enhanced stack

Post-stack migration was performed employing Kirchhoff time-migration (code from CREWES consortium). The migrated version of the NMO-stack in Figure 5-4 is shown in Figure 5-13. The image represents a well-focused reconstruction of both the reflections and the diffractions.

Correspondingly, the migrated results of the two diffraction-enhanced stacks from Figure 5-9 are shown in Figure 5-14. The zoomed versions of the images in Figure 5-14 show well-focused scattering energy. However, a closer inspection reveals that each focus seems to split in a positive and negative part. The distortions are made by a phase shift of $\sqrt{i} = 45^\circ$ in the migration code from CREWES.

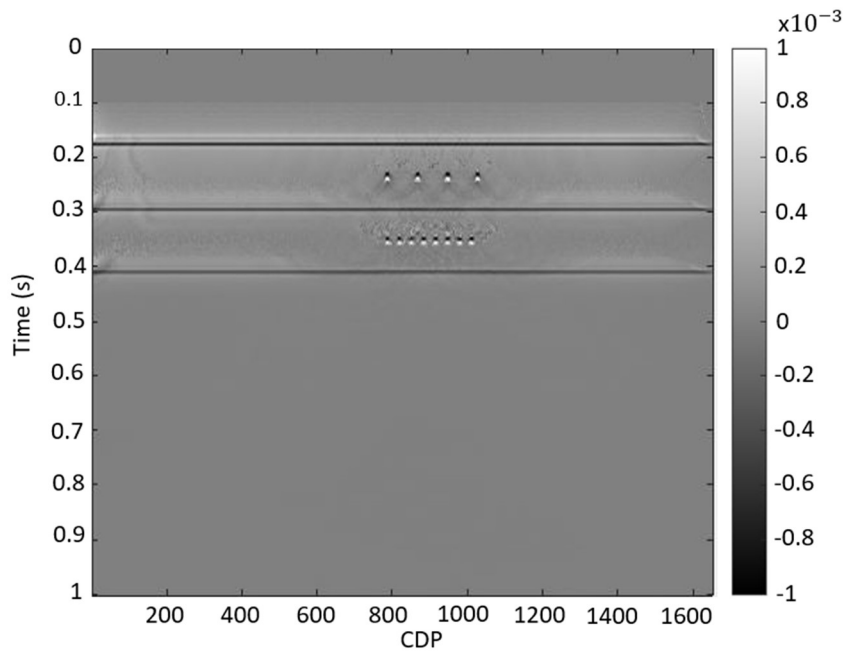


Figure 5-13: Time-migrated NMO-stack.

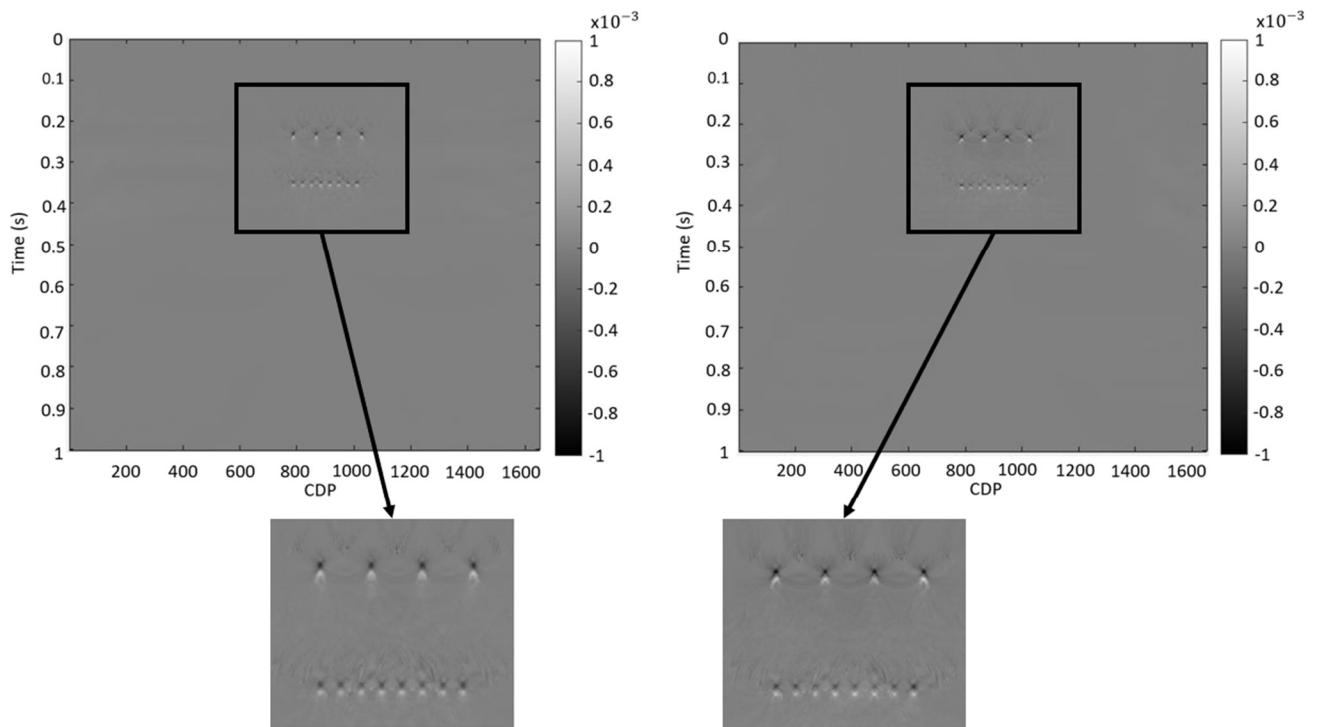


Figure 5-14: Migrated versions of the diffraction-enhanced stacks in Fig.5-9 with apertures of Δm 1500 and Δh 500. «Endrias» option (left) and «Vemund» option (right)

Combined stack

The migration of the combined stack corresponding to $\alpha = 0.8$ is shown in Figure 5-15 for both thresholding options. In comparison with Figure 5-13, the new results show a more balanced image between the reflections and diffractions.

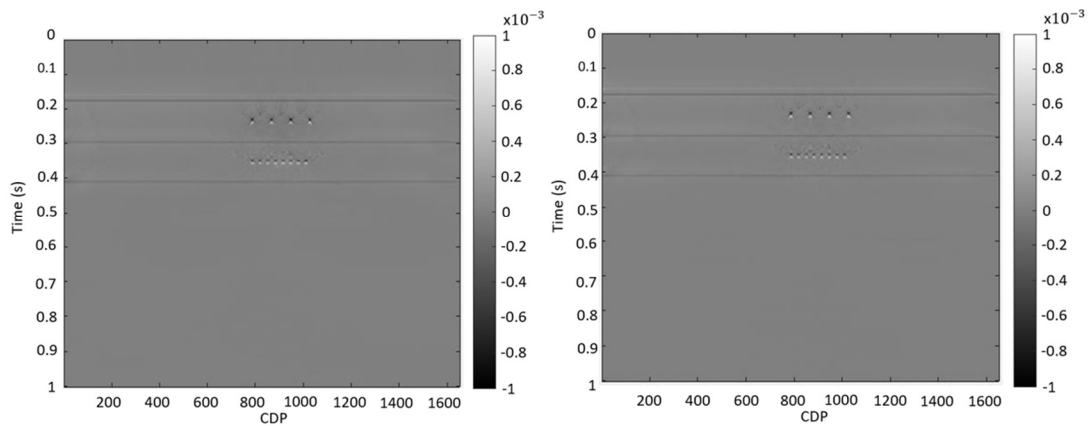


Figure 5-15 Migrated versions of the combined stacks ($\alpha=0.8$) in Figure 5-12. «Vemund» option (left) and «Endrias» option (right)

5.2 SIGSBEE 2A

The SIGSBEE 2A is a synthetic 2D dataset that was generated by the Subsalt Multiples Attenuation and Reduction Technology Joint Venture (SMAART JV, 2001). This acoustic marine dataset consists of a single seismic profile (Bauer, 2014) and represents measurements associated with a complex sub-surface in deep-water of the SIGSBEE Escarpment in the Gulf of Mexico (Paffenholz & BHP Petroleum, 2002). The main characteristic of the SIGSBEE Escarpment is the large salt structure. Thus, this controlled data set represents a realistic test of diffraction separation based on the DSR operator due to its complexity. Especially the rough shape of the salt body is expected to generate much-diffracted energy (Javed, 2012).

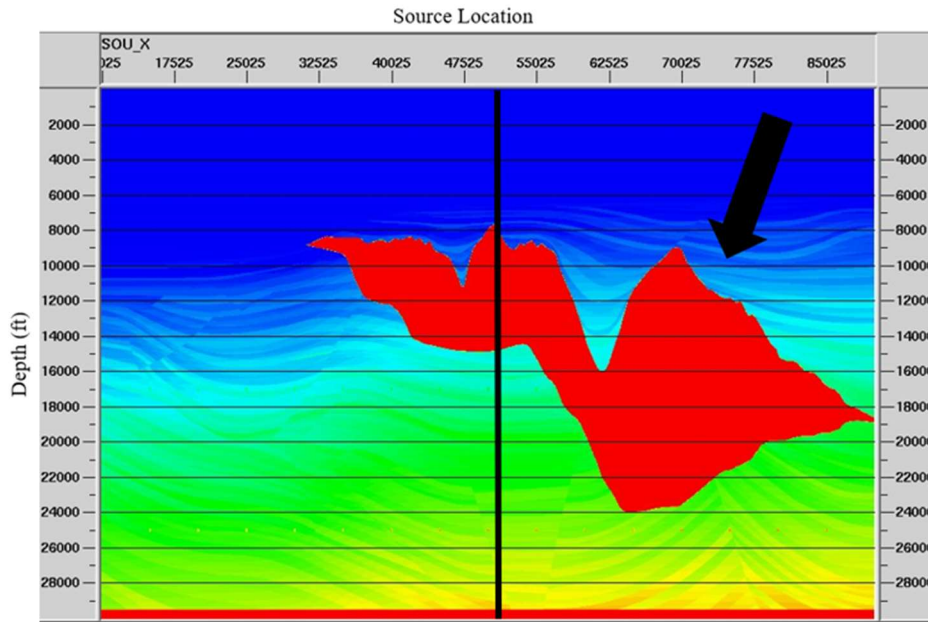


Figure 5-16: Velocity-depth model of the SIGSBEE 2A dataset. The black arrow indicates the salt structure and only the data on the right side of the black line is used. Note also that the depth is in feet. From (SMAART JV, 2001)

Figure 5-16 shows the velocity model of the SIGSBEE 2A dataset that (SMAART JV, 2001) has released. In this thesis, only a specific area is in use because the data is too large, and it is not necessary to run the whole data. The black arrow indicates the salt structure and it is associated with rough edges. These edges will create diffracted energy. The area of the salt body and the areas around are the area of interest. The better stack and velocity model in the time of the area of interest is present in the section below. The parameter of the dataset is in Table 5-1.

Minimum offset	0	Maximum offset	≈ 7932m (26025 ft)
Number of shots	500	Shot spacing	≈ 46m (150 ft)
Number of receivers	348	Receivers spacing	≈ 23m (75 ft)
Number of CMPs	2053	CMP spacing	≈ 12m (37.5 ft)
Recording time	12s	Sampling interval	8ms

Table 5-1: Key model parameters of the SIGSBEE 2A dataset. (Bauer, 2014)

5.2.1 Workflow

The workflow employed for the SIGSBEE 2A data set is given in Figure 5-17. It has much in common with the basic workflow introduced in Chapter 3, except for some slight modifications represented by the blue boxes. Since interval velocities in-depth already existed for this data set, stacking velocities in time could be obtained from Dix conversion. This processing step was carried out using CREWES. To obtain more optimized stacking results, these stacking velocities were slightly smoothed as shown in Figure 5-18 (right). Based on these smooth stacking velocities, both initial C parameters, as well as an NMO-stack, could be easily computed. Since the original units were in *feet*, a conversion to *meter* was also included in the preprocessing steps.

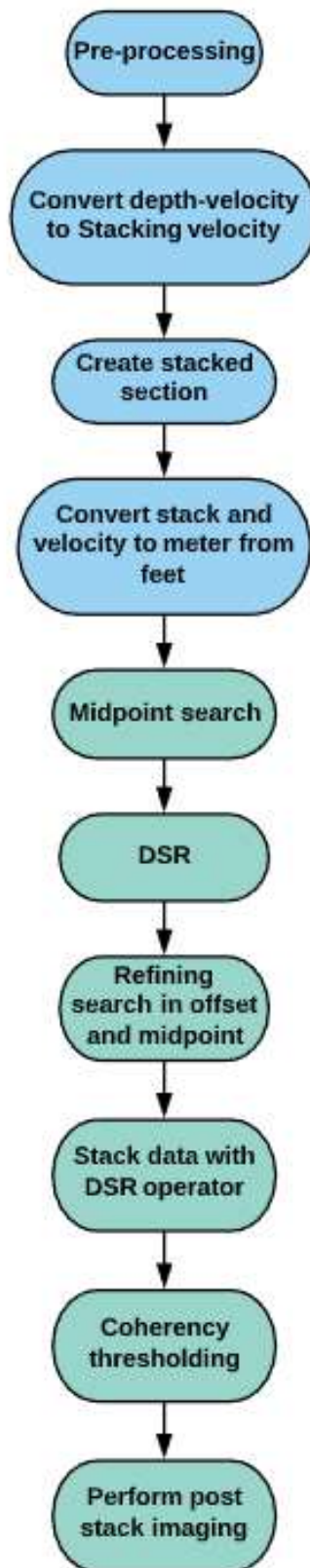


Figure 5-17: Workflow of the SIGSBEE dataset. Note: the only differences from the workflow in Figure 3-1 are represented by the blue boxes.

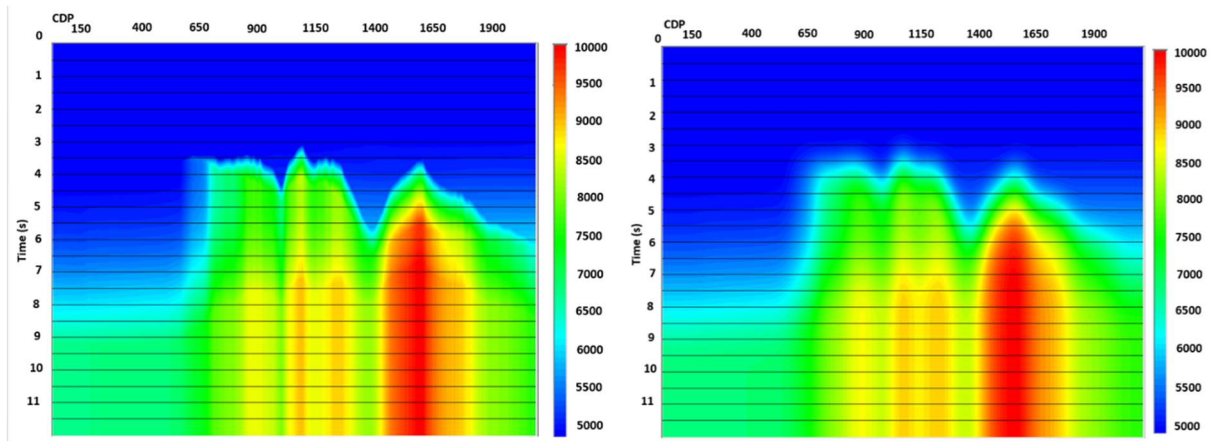


Figure 5-18: Stacking velocity field before (left) and after (right) applying smoothing. Note: the velocities are in feet in these plots.

Differences in NMO-stacking quality using the two different sets of stacking velocities from Figure 5-18 can be found by comparing Figure 5-19 and Figure 5-20. The use of the smoothed velocity field as shown in Figure 5-20 gives an overall improved quality as compared to the use of the raw velocity shown in Figure 5-19. Two examples of improvement are represented by the area within the red box and also the diffraction pointed by the arrow.

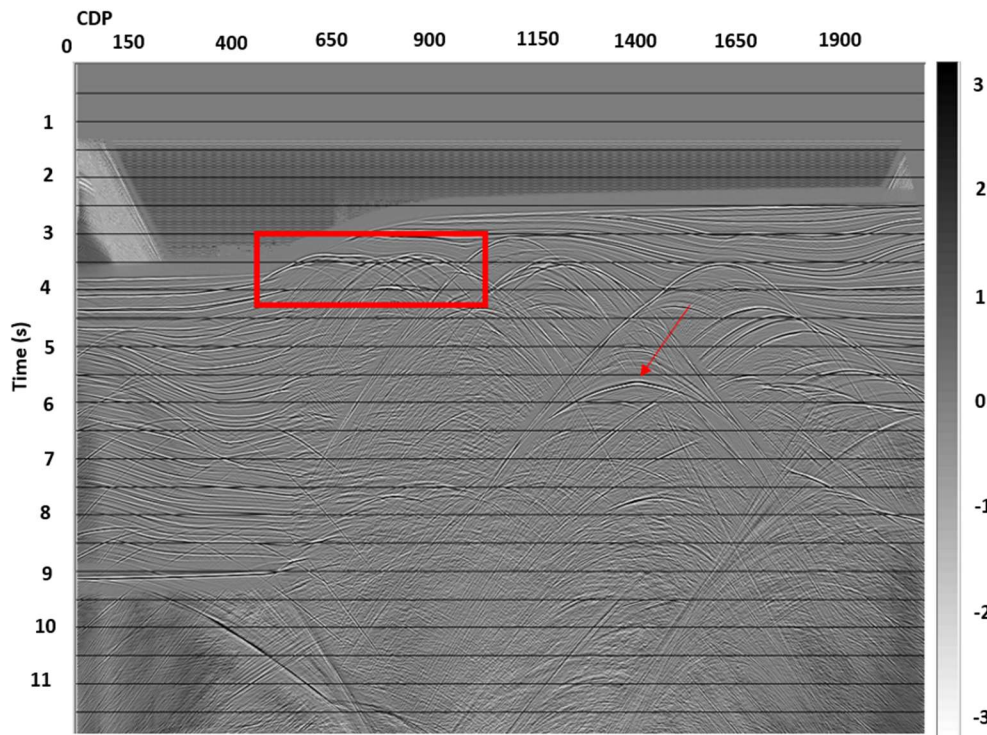


Figure 5-19: NMO-stack based on raw stacking velocities.

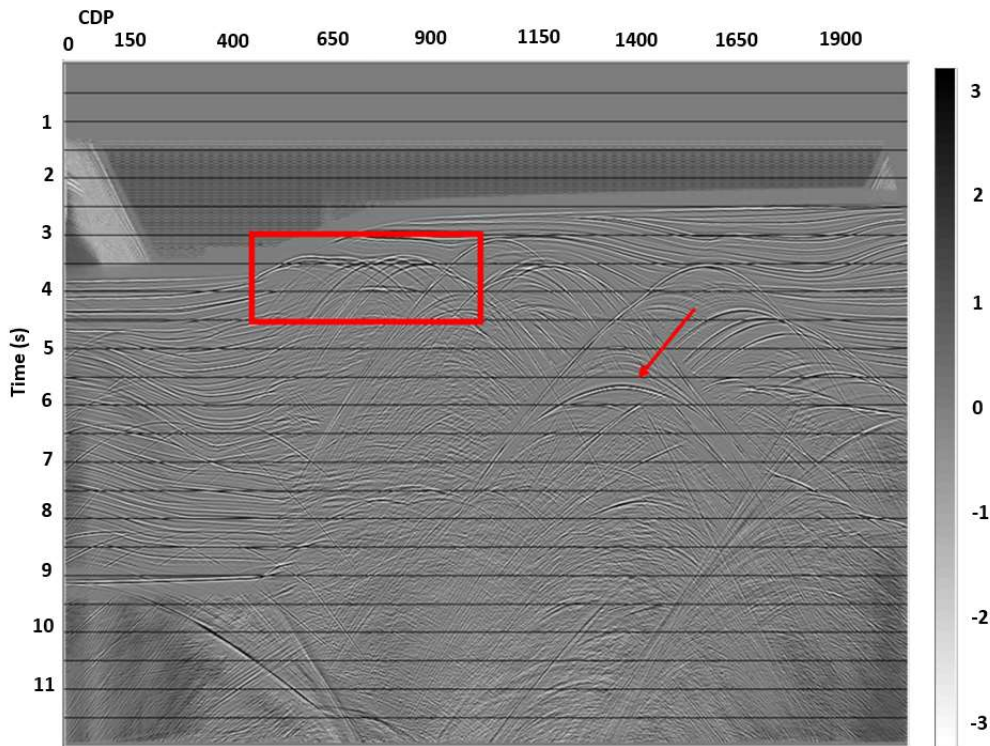


Figure 5-20: NMO-stack based on smoothed stacking velocities.

Until now, examples shown correspond to the complete model. As already mentioned, only the right part of the model in Figure 5-16 will be considered further to reduce the computational burden of the diffraction separation process. Figure 5-21 (left) and Figure 5-21 (right) show respectively the NMO stack for the selected part and the corresponding smoothed stacking-velocity model. It follows that the highest stacking velocity is about 3000 m/s. Note that the velocity unit has now been converted from feet/sec to m/sec.

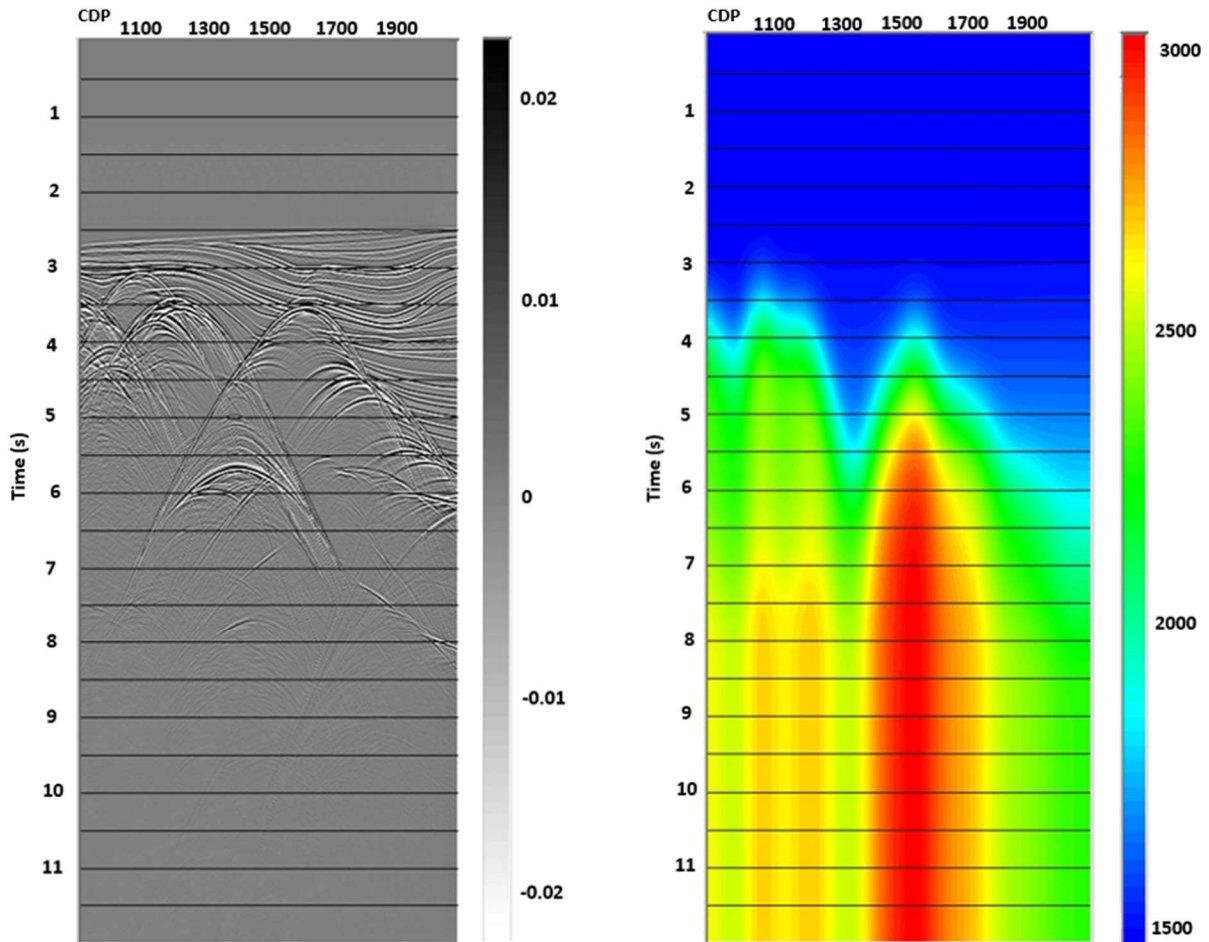


Figure 5-21: NMO-stack for selected part of the model (left) and corresponding stacking-velocity model of the interest area.

It should be noted that all major results for the SIGSBEE 2A model have been plotted using ProMax to ensure high quality.

5.2.2 Separation results

In this subsection, only separation results corresponding to the best choice of apertures of 1500 (Δm) and 500 (Δh) are shown. Results for two other choices of mid-point aperture, e.g. 800m and 1200m can be found in Appendix C.

Figure 5-22 (left) shows the panel of parameter A obtained after semblance analysis in the mid-point domain and with the corresponding semblance plot given to the far right. The subfigure in the middle is the panel of parameter C after updating. The semblance shows high values at apexes of diffractions and decreases along their flanks. This is the same trend as observed in the simpler model in Section 5.1.

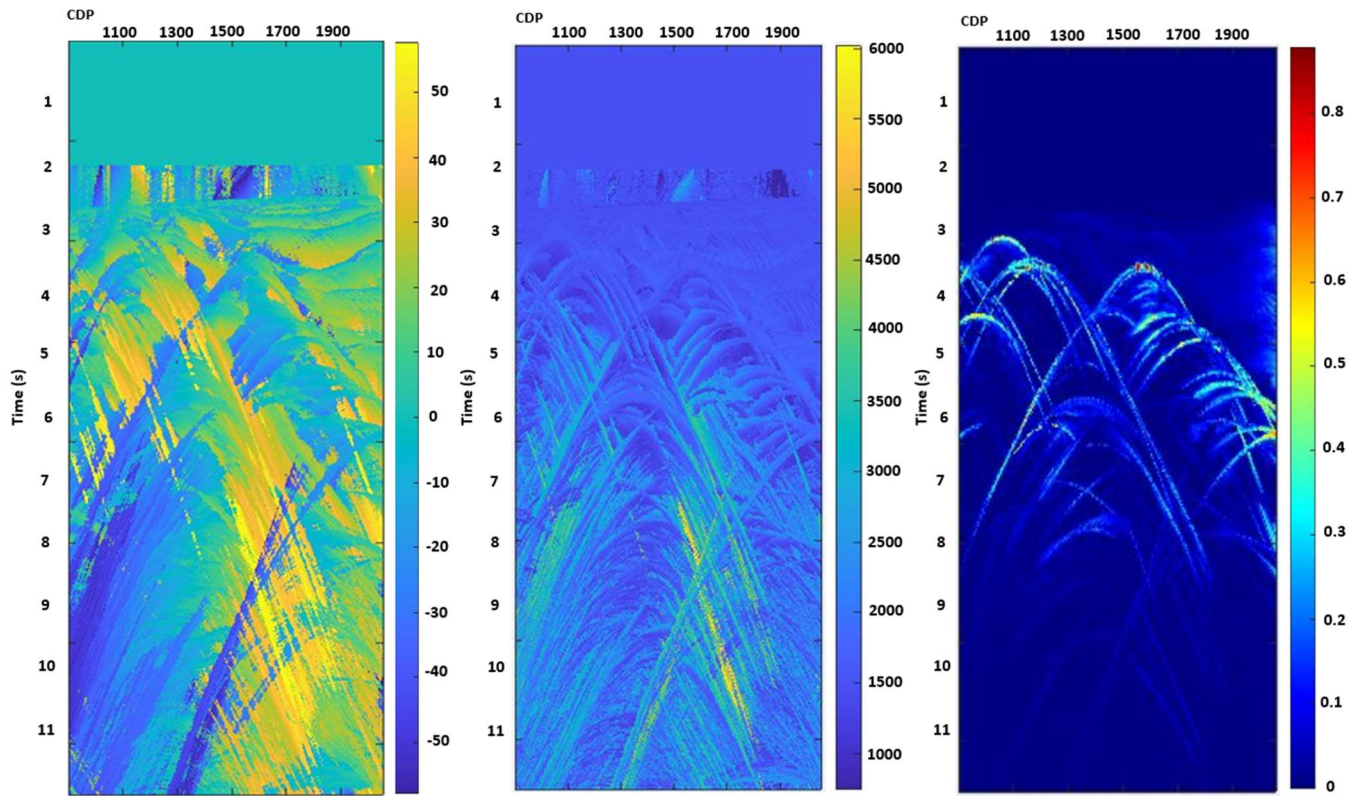


Figure 5-22: Parameter A (left), C (middle) and semblance (right) from midpoint search

After the intermediate result obtained in Figure 5-22, a multi-domain refinement step followed. The semblance in mid-point after this adjustment is shown in Figure 5-23. Direct comparison between Figure 5-22 (far right) and Figure 5-23 demonstrates that the semblance after refinement has fewer noise artifacts.

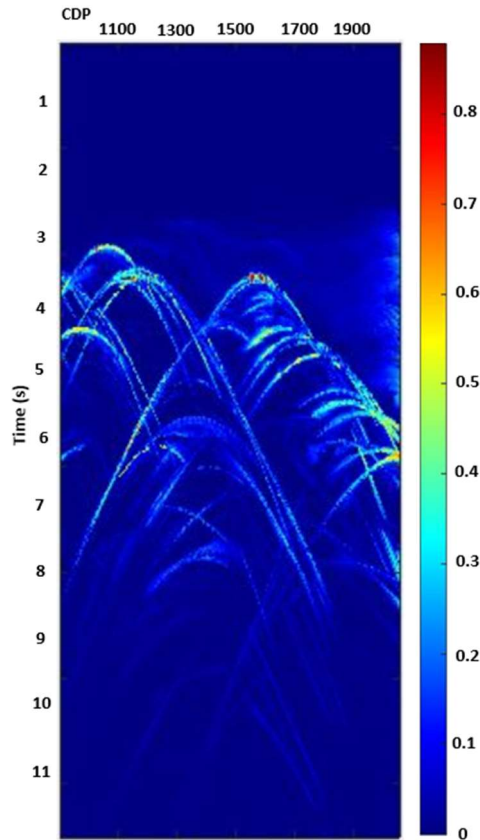


Figure 5-23: Semblance in midpoint after multi-domain refinement for SIGSBEE model

After optimal parameters A and C have been obtained for the DSR operator, a raw diffraction-enhanced stack can be formed as shown in Figure 5-24. Without any thresholding applied, some reflection residuals are still visible as expected. Correspondingly, Figure 5-25 (left) and (right) show the diffraction-enhanced stacks after thresholding (respectively «Vemund» and «Endrias» options). The threshold value for the «Vemund» option was 0.1.

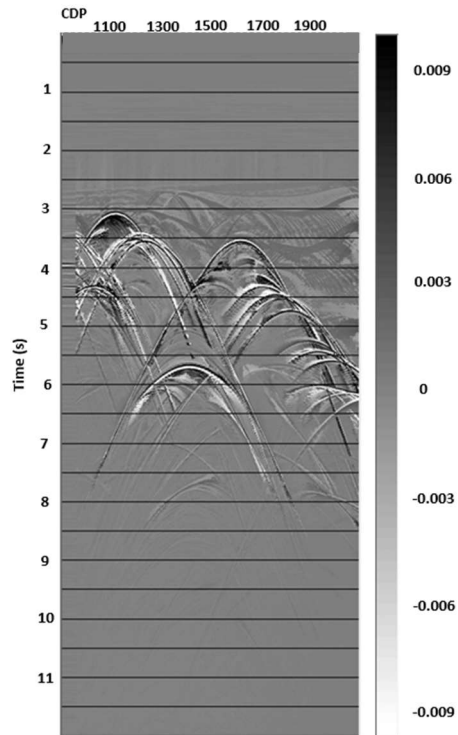


Figure 5-24: DSR stack before thresholding for SIGSBEE data

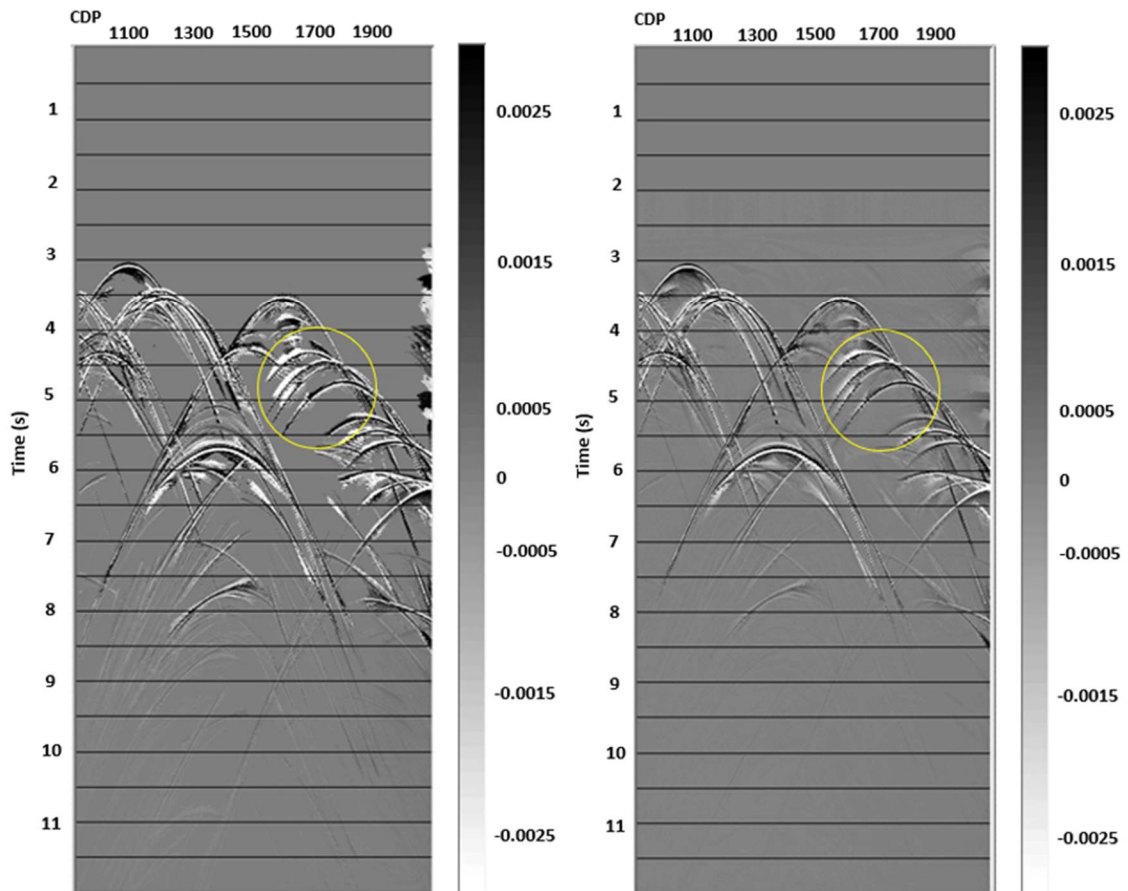


Figure 5-25: DSR stacks after thresholding. (left) «Vemund» option and (right) «Endrias» option

A direct comparison between the two DSR stacks in Figure 5-25 shows that the thresholding has worked well for both strategies. There is a somehow cleaner separation in the «Vemund» result, where the reflections efficiently removed. Although the separation process has performed overall well, diffractions within the marked area of a yellow circle have lost some parts of their flanks. The «Vemund» option shows more noise around the diffraction apexes and loses parts of the data. Likewise, the «Endrias» stack represents a good separation and with somewhat less noise and slightly sharper diffractions. Thus, it can be concluded that the «Endrias» approach shows a slightly better separation than the «Vemund» option.

Finally, the time-migration of the diffraction-enhanced stacks in Figure 5-25 was post-stack time-migrated. The results for the two thresholding options are shown in Figure 5-26 (left) and Figure 5-27 (left). On direct comparison, the migrated result corresponding to the «Endrias» option seemed to perform best. The upper boundary of the salt structure is fairly well recovered, but its lower part is distorted. This is as expected since time-migration is employed. If the image below the salt is to be trusted, depth migration needs to be used.

A combined section was also formed from the NMO and diffraction-enhanced stacks employing a weight factor of 0.8. The corresponding results obtained for the two thresholding options are shown in Figure 5-26 (right) and Figure 5-27 (right). Again, the «Endrias» option scores highest and it also seems that the combined section gives a slightly improved image of the upper salt boundary.

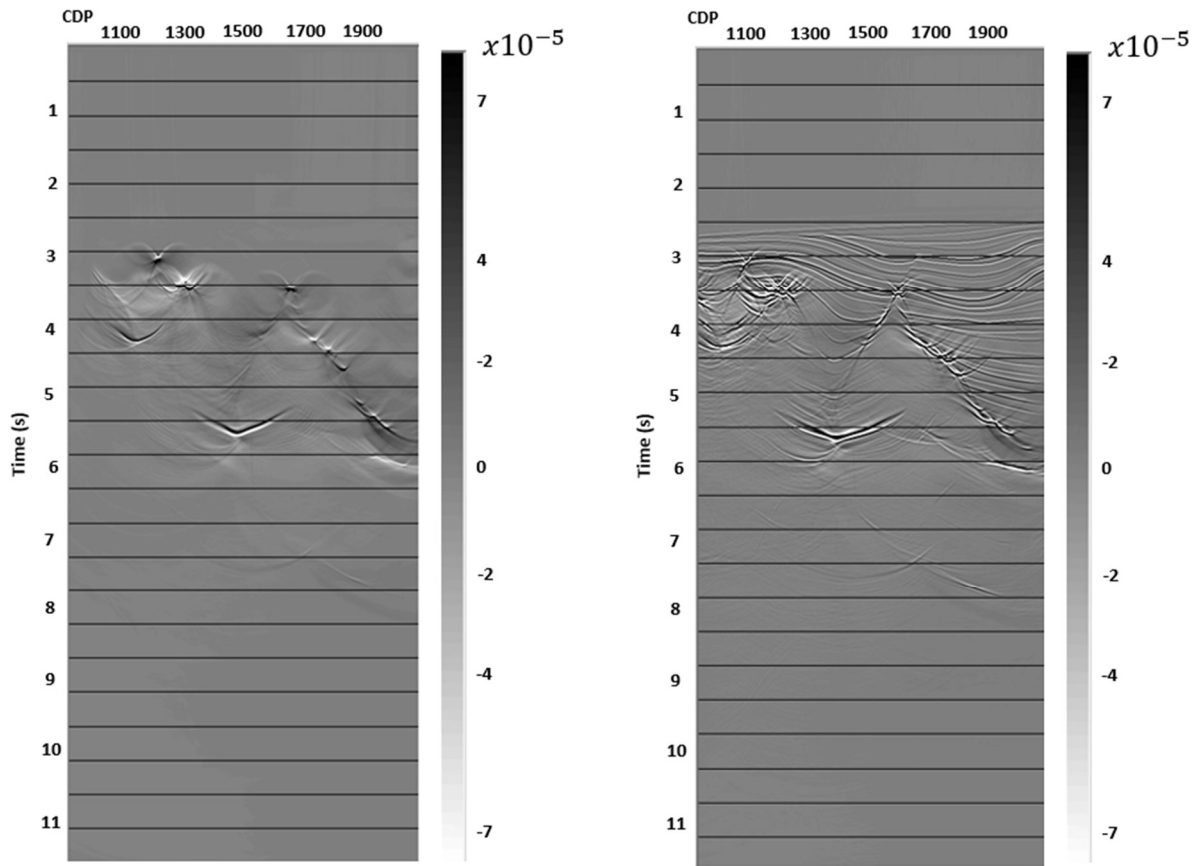


Figure 5-26: Migration of diffraction-enhanced stack (left) and (right) combined stack – «Endrias» option

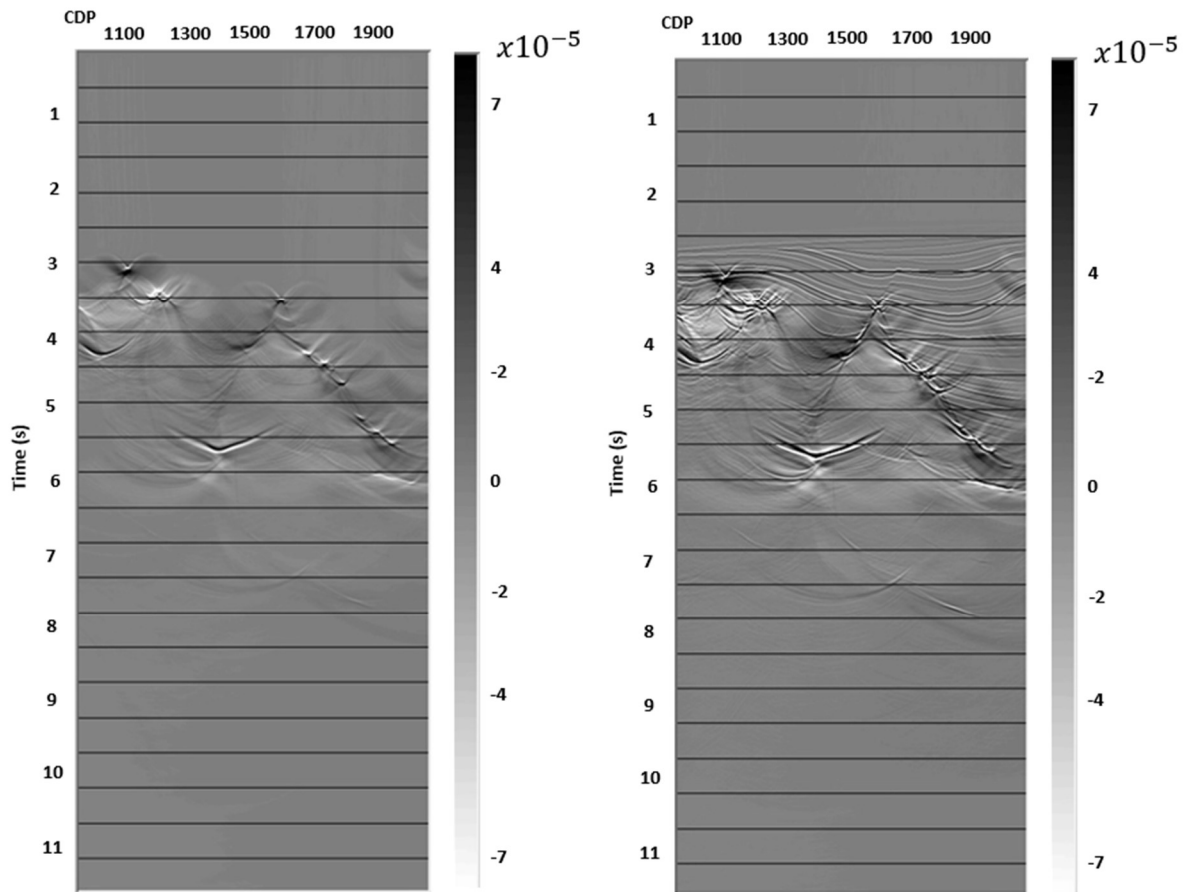


Figure 5-27: Migration of diffraction-enhanced stack (left) and combined stack (right) – «Vemund» option

6 Discussion

6.1 Simple scattering model

The simple scattering model introduced in Section 5.1 was used as a demonstration of the resolution capability of the DSR technique. Two chains of point scatterer (one with 4 and one with 8) were embedded in a layered subsurface model. The scattering strength of each diffraction point was fairly weak (10% of the surrounding contrast). The use of the proposed workflow for diffraction enhancement gave a raw diffraction stack with some residual artifacts from the reflections. However, after proper thresholding, a very good separation was obtained.

As discussed earlier, two different approaches of thresholding labeled respectively «Vemund» and «Endrias» were tested. In both cases the semblance panel is employed, although in a somewhat different way. The «Endrias» option implies multiplying the raw diffraction-enhanced stack with the semblance. Correspondingly, the «Vemund» option implies removing all values in the raw diffraction-enhanced stack where the corresponding semblance value is below a user-defined threshold. Several tests were carried out to determine the optimal value of this threshold, and a value of 0.43 was found to work well.

Determining the optimal aperture valued in offset and mid-point is crucial for the DSR technique to perform well. The offset aperture should be chosen fairly small to comply with the underlying paraxial assumption. This is under the small spread assumption in conventional NMO stacking. After some initial testing, a value of 500m seemed to work well. The aperture in mid-point plays a much more crucial role. If this aperture is chosen too small, the separation result will be dominated by reflections. Thus, extensive testing had to be carried out to define an optimal value. As a good compromise between computational burden and quality in separation, an aperture in mid-point of 1200m was chosen.

The idea of a combined stack was also tested out for this scattering model. This implies that a new stack can be formed by adding the diffraction-enhanced stack and the conventional NMO stack employing proper weighting. In this way, a more balanced stack between reflections and diffractions may be obtained. Several tests changing the scale factor α were carried out, and a value of 0.8 was found to give the best result.

Post-stack time-migration of the Kirchhoff type was performed on all the various stacks leading to high-resolution images of the model in all cases of input.

6.2 SIGSBEE 2A

The SIGSBEE 2A data set represents a much more realistic model case due to its high degree of complexity. Thus, the use of this model will serve as a test of the capability of the DSR technique to handle seismic field data. The large advantage of using controlled data and not field data in such testing is in the case of the former the actual subsurface model is known in all details.

The SIGSBEE 2A data set is quite large so only approximately half of the total data volume was employed in the testing. The reason being that the semblance-based diffraction separation process is rather time-consuming. However, the selected area contained most of the salt body being the target object in this analysis. Due to the roughness of the salt boundary, a fairly large amount of diffractions were expected to be present.

As part of the data set, a depth-velocity model is also provided. By the use of CREWES, a Dix type of conversion to stacking velocities in time was performed. After proper smoothing, this velocity field serves as the initial model for the parameter C. Moreover, a stacked section can be computed employing the stacking-velocity field. It was demonstrated that without a proper smoothing of the stacking velocities, artifacts are present in the NMO stack. This is especially noticeable for diffractions.

The raw DSR stack (e.g. before thresholding) was quite noisy and with clear traces of reflections. After thresholding, both uses of the «Vemund» option and the «Endrias» option gave good separations. However, on direct comparison, the «Endrias» approach seemed overall better with less noise around the separated diffractions. The time-migrated results of the two thresholded diffraction stacks gave a fairly good reconstruction of the upper boundary of the salt body. Especially the parts associated with some degree of roughness are recovered as expected. The image of the lower boundary of the salt and structures below in general will be distorted. This is caused by the use of time-migration instead of depth-migration.

A combined stack was also formed for this data set using the same weighting as in Section 6.1. The migrated result seemed to give a slightly better image of the upper salt boundary with some reflected energy filling in where the smoothness of the salt boundary is high.

7 Conclusions and further work

The use of the DSR operator to separate diffractions from reflections has been investigated for both simple and more complex controlled models. For the method to perform well the following issues need to be addressed:

- Optimal apertures in offset and mid-point need to be determined. This step represents the most crucial part of the separation process. The aperture in offset should be selected according to the small spread assumption. The aperture in mid-point needs to be large enough to minimize contributions from reflections.
- The choice of the search strategy is a challenge in general. If the full parameter space should be sampled during the semblance analysis, the computational burden will be prohibitively large. Thus, a pragmatic approach is better suited by considering the offset and mid-point space separately except for a final multi-domain adjustment. The use of the analytical link between parameters A and C also constrain the search.
- The raw diffraction-enhanced stack will be contaminated by traces of reflected energy, even for the simpler models. Thus, semblance based thresholding should always be employed.

Further work

- An improved approach for determining aperture in mid-point based on Fresnel zone calculations (depth-dependent).
- Application of the proposed workflow on field data.
- Investigate further improvements in the computational speed of the separation process. This could include data more sparsely sampled in both time and space as input since diffractions unlike reflections have a large Fresnel zone. An example of such an approach is the use of concepts from holography as briefly discussed by Thorkildsen (2019).

8 References

- Asgedom, E. G., Gelius, L. J., & Tygel, M. (2012a, May). Seismic Coherency Measures in Case of Interfering Events: A Focus on the Most Promising Candidates of Higher-Resolution Algorithms. *Signal processing magazine*(56), pp. 47-56. Retrieved December 2019, from <https://ieeexplore.ieee.org/document/6179813>
- Asgedom, E. G., Gelius, L. J., Faccipieri, J., & Tygel, M. (2012b, September). 2D pre- and post-stack diffraction separation and imaging. *SEG*. Retrieved November 2019, from <https://library.seg.org/doi/pdf/10.1190/segam2012-0655.1>
- Asgedom, G. E., Gelius, L. J., & Tygel, M. (2011, August). Diffraction separation using the CRS technique: A field data application. *SBGf*, pp. 976-979. Retrieved November 2019, from <https://library.seg.org/doi/pdf/10.1190/sbgf2011-202>
- Bauer, A. (2014). *From zero-offset to common-offset with diffractions*. Master's thesis, University of Hamburg, Institute of Geophysics. Retrieved May 2020, from https://www.researchgate.net/publication/301492945_From_zero-offset_to_common-offset_with_diffractions
- Dell, S., & Gajewski, D. (2011, September-October). Common-reflection-surface-based workflow for diffraction imaging. *Geophysics*, 76(5), pp. 187-195. doi:10.1190/GEO2010-0229.1
- Faccipieri, J. H., Coimbra, T. A., Gelius, L. J., & Tygel, M. (2016, July). Stacking apertures and estimation strategies for reflection and diffraction enhancement. *Geophysics*, 81(4), pp. 271-282. Retrieved January 29, 2020, from <https://doi.org/10.1190/geo2015-0525.1>
- Gazdag, J., & Sguazzero, P. (1984, October). Migration of seismic data. *Proceedings of the IEEE*(10), pp. 1302-1307. doi:10.1109/PROC.1984.13019
- Hertweck, T., Schleicher, J., & Mann, J. (2007, July). Data stacking beyond CMP. *The Leading Edge*, 26(7). doi:<https://doi.org/10.1190/1.2756859>

- Javed, M. W. (2012). *Separation of reflections from diffractions using the CRS-technique*. Master's thesis, University of Oslo, Department of Geosciences. Retrieved April 2020, from <https://www.duo.uio.no/handle/10852/12637>
- Kanasewich, E. R., & Phadke, S. M. (1988, March). Imaging discontinuities on seismic sections. *Geophysics*, 53(3), pp. 334-345. doi:10.1190/1.1442467
- Levin, F. K. (1971, June). Apparent velocity from dipping interface reflections. *Geophysics*, 36(3), pp. 510-516. Retrieved January 2020, from <https://doi.org/10.1190/1.1440188>
- Lima, E., Santos, L. T., Schleicher, J., & Tygel, M. (2011, March). A comparison of semblance of different order in common-reflection-surface parameter estimation. *Journal of Geophysics and Engineering*, pp. 175-184. doi:10.1088/1742-2132/8/2/005
- Mann, J., Schleicher, J., & Hertweck, T. (2007, June). CRS stacking - A Simplified Explanation. *EAGE*, pp. 1-5. Retrieved January 2020, from https://www.juergenmann.de/Abstracts/MannSchleicherHertweck_EAGE07.pdf
- Margrave, G. F. (2020). CREWES Matlab Toolbox. Retrieved May 2020, from <https://www.crewes.org/ResearchLinks/FreeSoftware/>
- Nucleus-Help. (2020). *PGS-Nucleus-Program --> help function*. Retrieved January 2020
- Paffenholz, J., & BHP Petroleum. (2002, January). Sigsbee2 synthetic subsalt dataset: image quality as function of migration algorithm and velocity model error. pp. 1-4. Retrieved May 2020, from https://www.researchgate.net/publication/237542977_Sigsbee2_synthetic_subsalt_dataset_image_quality_as_function_of_migration_algorithm_and_velocity_model_error
- Schlumberger. (2020). Common midpoint. (S. Limited, Ed.) Retrieved January 2020, from https://www.glossary.oilfield.slb.com/Terms/c/common_midpoint.aspx
- SMAART JV. (2001, September). Sigsbee2a/ Data Release. Retrieved June 2020
- Thorkildsen, V. S. (2019). *Separation of diffractions by diffraction-stacking and plane-wave destruction filtering*. Master's thesis, University of Oslo, Department of Geosciences, Oslo. Retrieved from <https://www.duo.uio.no/handle/10852/70025>

Waldeland, A., Zhao, H., Faccipieri, J., Schistad Solberg, A., & Gelius, L.-J. (2018, January-February). Fast and robust common-reflection-surface parameter estimation. *Geophysics*, 83(1), pp. 1-13. doi:10.1190/GEO2017-0113.1

APPENDIX

APPENDIX A:

Derivation of the DSR equation

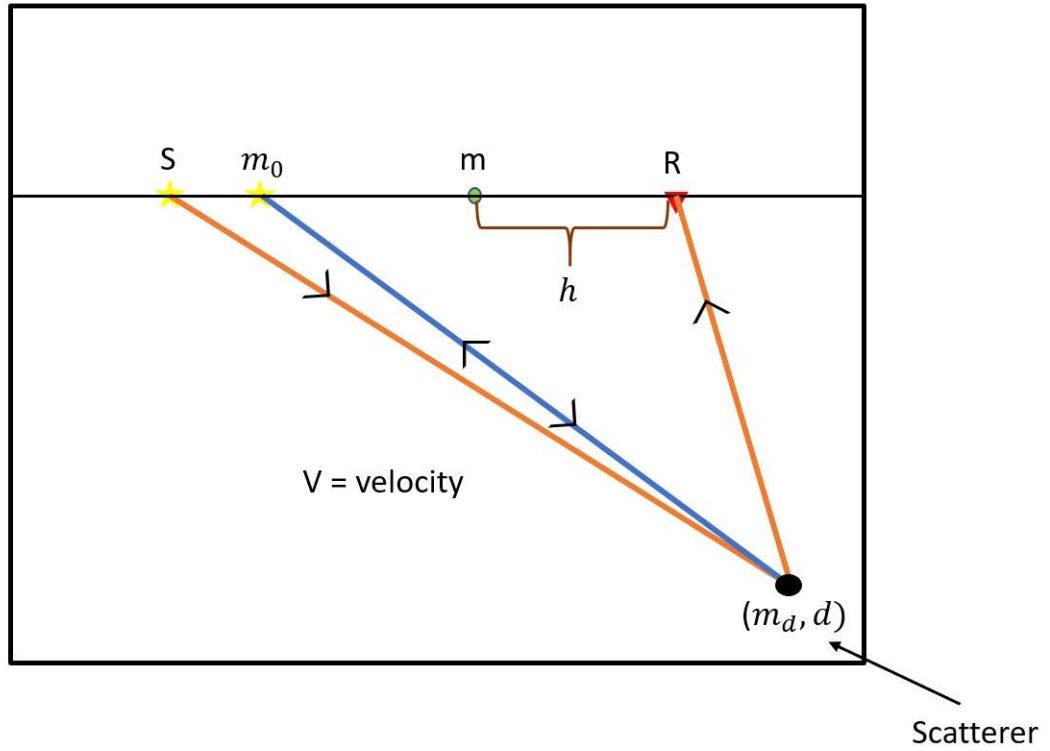


Figure A-1: a schematics of the geometry where the "d" is the depth of the scatterer

Traveltime for paraxial (the orange ray in Figure A-1) ray, $S \rightarrow$ scatterer $\rightarrow G$

$$t(m, h) = \sqrt{\frac{(m_d - m + h)^2 + d^2}{V^2}} + \sqrt{\frac{(m_d - m - h)^2 + d^2}{V^2}} \quad (\text{A-1})$$

Traveltime for reference (the blue ray in Figure A-1) ray, (Z_0 , midpoint m_0)

$$t_0(m_0, 0) = 2\sqrt{\frac{(m_d - m_0)^2 + d^2}{V^2}} \quad (\text{A-2})$$

Then we introduce $\Delta m = m - m_0$ and rewrite Equation (A-1) with the use of Equation (A-2)

$$\begin{aligned}
t(m, h) &= \sqrt{\frac{[(m_d - m_0) - (\Delta m - h)]^2 + d^2}{v^2}} + \sqrt{\frac{[(m_d - m_0) - (\Delta m + h)]^2 + d^2}{v^2}} \\
t(m, h) &= \sqrt{\frac{(m_d - m_0)^2 - 2(m_d - m_0)(\Delta m - h) + (\Delta m - h)^2 + d^2}{v^2}} + \sqrt{\frac{(m_d - m_0)^2 - 2(m_d - m_0)(\Delta m + h) + (\Delta m + h)^2 + d^2}{v^2}} \\
t(m, h) &= \sqrt{\frac{1}{4}t_0^2 - \frac{2(m_d - m_0)(\Delta m - h)}{v^2} + \frac{(\Delta m - h)^2}{v^2}} + \sqrt{\frac{1}{4}t_0^2 - \frac{2(m_d - m_0)(\Delta m + h)}{v^2} + \frac{(\Delta m + h)^2}{v^2}} \quad (\text{A-3})
\end{aligned}$$

The next step is to define A to further use it in Equation (A-3)

$$A = -4 \frac{(m_d - m_0)}{t_0 v^2} \quad (\text{A-4})$$

This gives,

$$\begin{aligned}
t(m, h) &= \frac{1}{2} \sqrt{t_0^2 + 2At_0(\Delta m - h) + \frac{4(\Delta m - h)^2}{v^2}} + \frac{1}{2} \sqrt{t_0^2 + 2At_0(\Delta m + h) + \frac{4(\Delta m + h)^2}{v^2}} \\
t(m, h) &= \frac{1}{2} \sqrt{t_0^2 + 2At_0(\Delta m - h) + A^2(\Delta m - h)^2 + \left(\frac{4}{v^2} - A^2\right)(\Delta m - h)^2} + \\
&\quad \frac{1}{2} \sqrt{t_0^2 + 2At_0(\Delta m + h) + A^2(\Delta m + h)^2 + \left(\frac{4}{v^2} - A^2\right)(\Delta m + h)^2} \\
t(m, h) &= \frac{1}{2} \sqrt{[t_0 + A(\Delta m - h)]^2 + C(\Delta m - h)^2} + \frac{1}{2} \sqrt{[t_0 + A(\Delta m + h)]^2 + C(\Delta m + h)^2} \quad (\text{A-5})
\end{aligned}$$

Where,

$$C = \frac{4}{v^2} - A^2 \quad (\text{A-6})$$

Appendix B:

Test of different mid-point apertures (simple scattering model)

In this Appendix, additional tests regarding the mid-point aperture are presented for the simple scattering model discussed in Section 5.1.

Two different parameterizations are shown below. In both cases, the aperture in offset is set to 500m. The aperture in mid-point is respectively 1000m and 1200m.

Aperture $\Delta m = 1000$ and $\Delta h = 500$

Figure B-1 shows the A and C parameter panels output from the semblance analysis. The corresponding semblance panel in mid-point is shown in Figure B-2. It can be seen that the semblance associated with the diffractions is fairly high and increasing along the flanks. However, also residuals are presently associated with reflections (especially toward boundaries). The brute-force diffraction-enhanced stack is given in Figure B-3 for both choices of thresholding. The threshold factor is set to 0.45 in the case of «Vemund». Independent of the choice of thresholding, artifacts due to reflections are present in both images in Figure B-4.

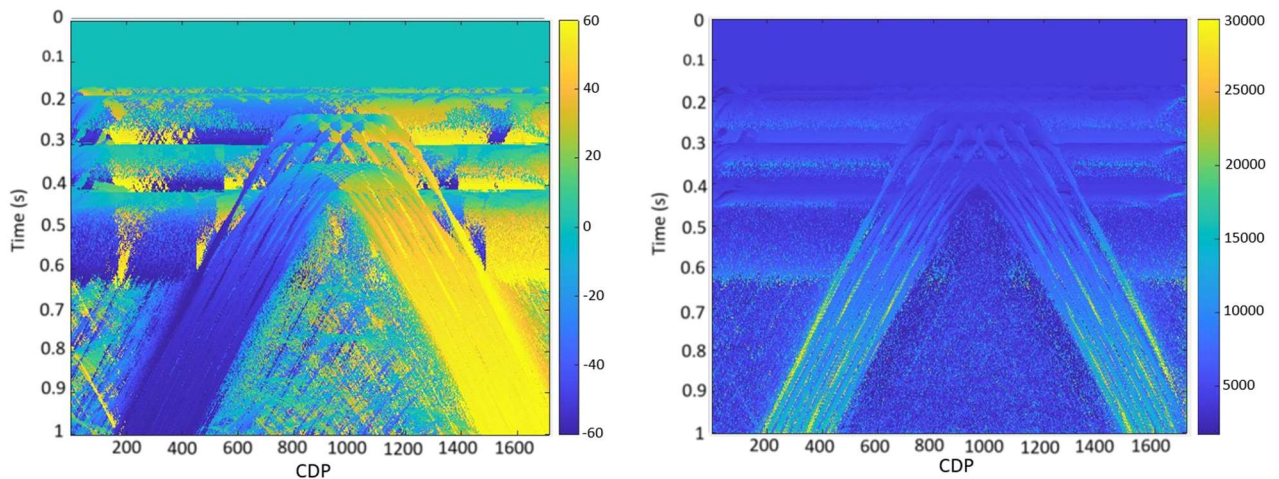


Figure B-1: A and C panels for apertures of Δm 1000 and Δh 500.

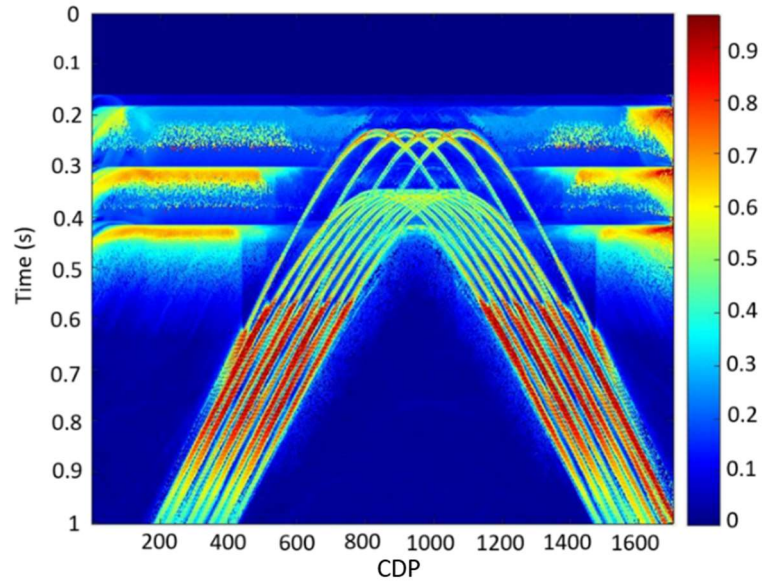


Figure B-2: Plot of semblance in mid-point

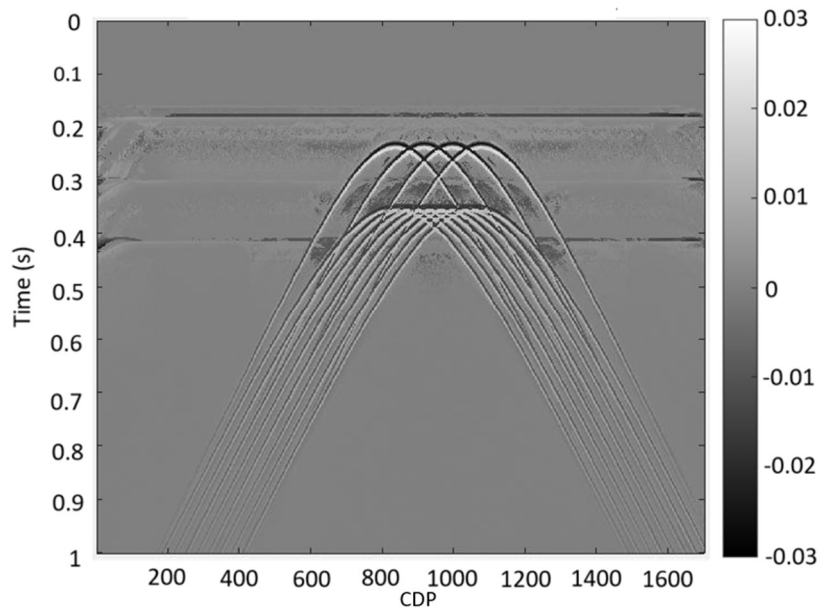


Figure B-3: Brute-force diffraction stack with apertures of Δm 1000 and Δh 500.

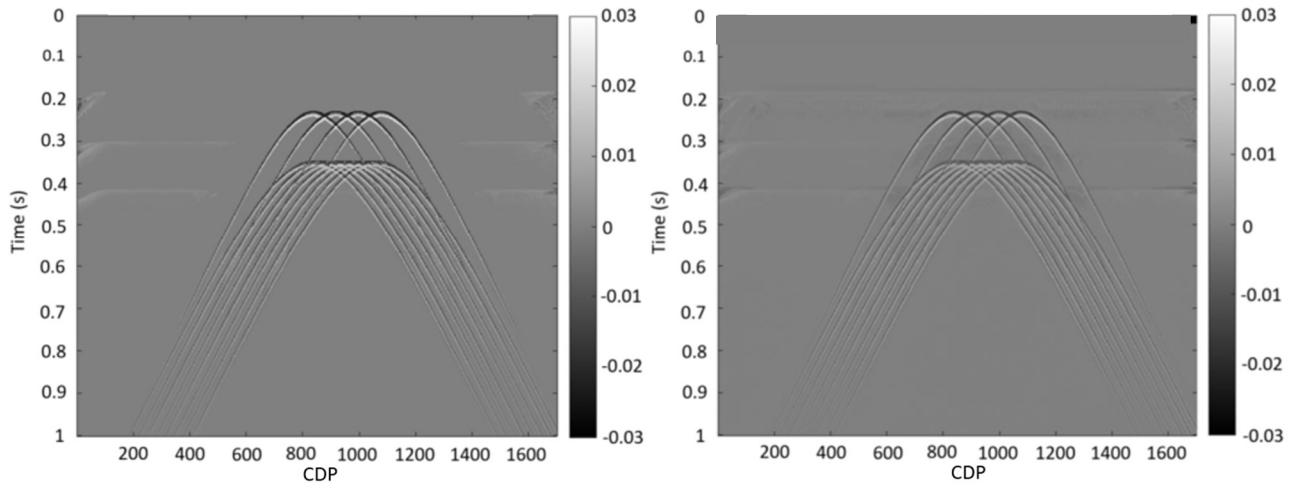


Figure B-4: Diffraction-enhanced stacks after (left) «Vemund» thresholding and (right) «Endrias» thresholding Aperture Δm 1200 and Δh 500

Aperture Δm 1200 and Δh 500

The counterpart of Figures B-1 to B-4 for the second aperture combination is given in Figures B-5 to B-8. The quality of the diffraction separation has improved slightly, but residuals caused by reflections are still present in the diffraction-stacks. Thus, a larger aperture in mid-point is needed in order to arrive on a cleaner separation result.

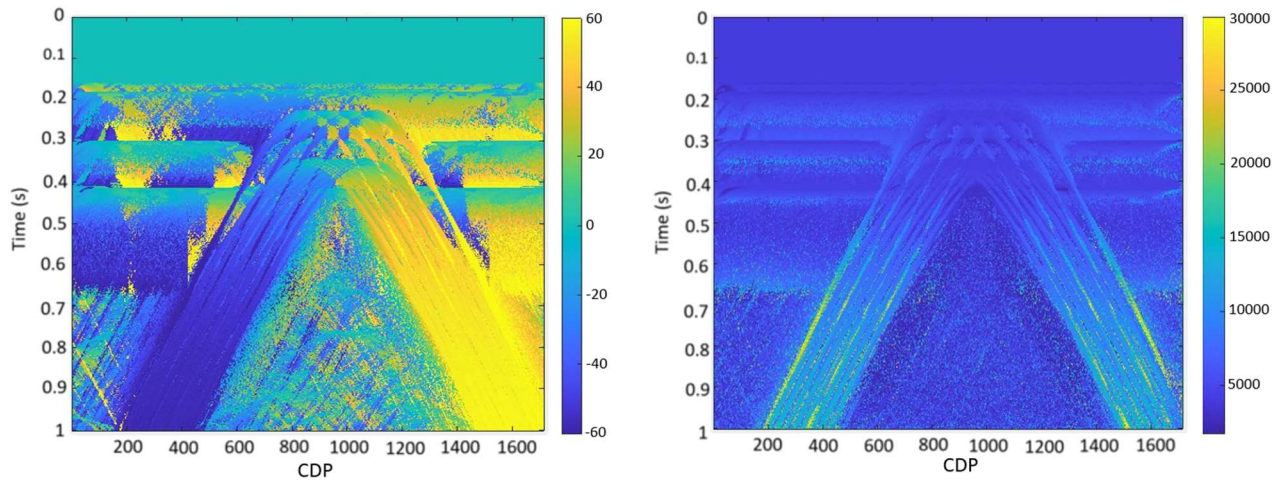


Figure B-5: A and C panels for apertures of Δm 1200 and Δh 500.

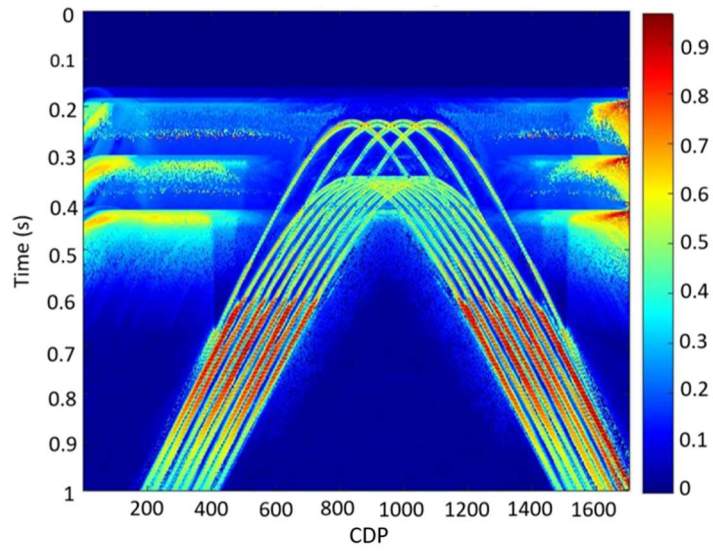


Figure B-6: Plot of semblance in mid-point

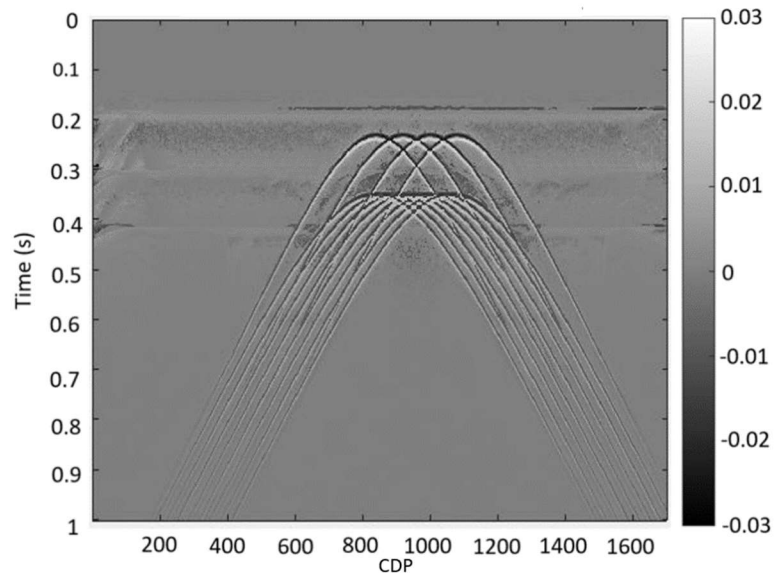


Figure B-7: Brute-force diffraction stack with apertures of Δm 1200 and Δh 500.

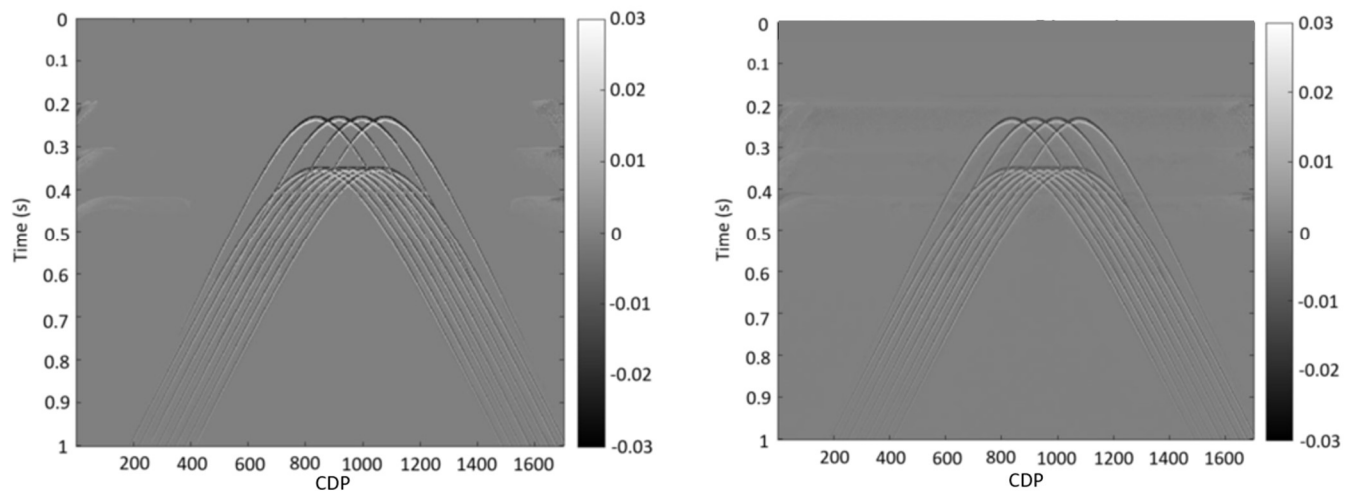


Figure B-8: Diffraction-enhanced stacks after (left) «Vemund» thresholding and (right) «Endrias» thresholding

APPENDIX C:

SIGSBEE 2A – Midpoint aperture of 800 and 1200

In this Appendix, additional tests regarding the mid-point aperture are presented for the SIGSBEE 2A model discussed in Section 5.2.

Two different parameterizations are shown below. In both cases, the aperture in offset is set to 500m. The aperture in mid-point is respectively 1200m (Figures C-1 and C-2) and 800m (Figures C-3 and C-4). It can be easily seen that the smallest aperture of 800m gives a poor result with a large amount of separation noise present. By increasing the mid-point aperture to 1000m, significant improvements are obtained but still with clear traces of reflection residuals.

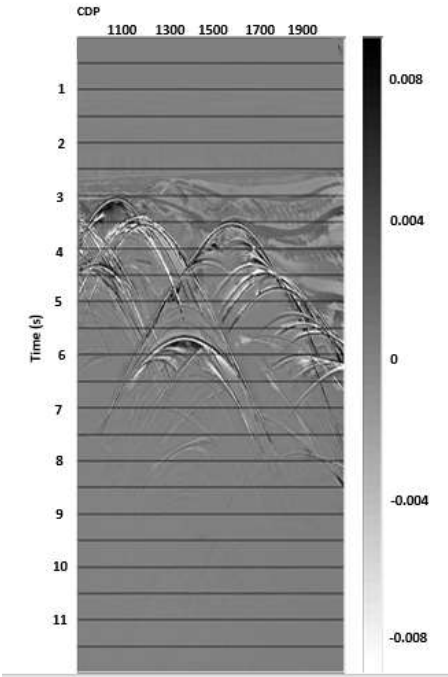


Figure C-1: DSR stack before thresholding for aperture Δm 1200 and Δh 500

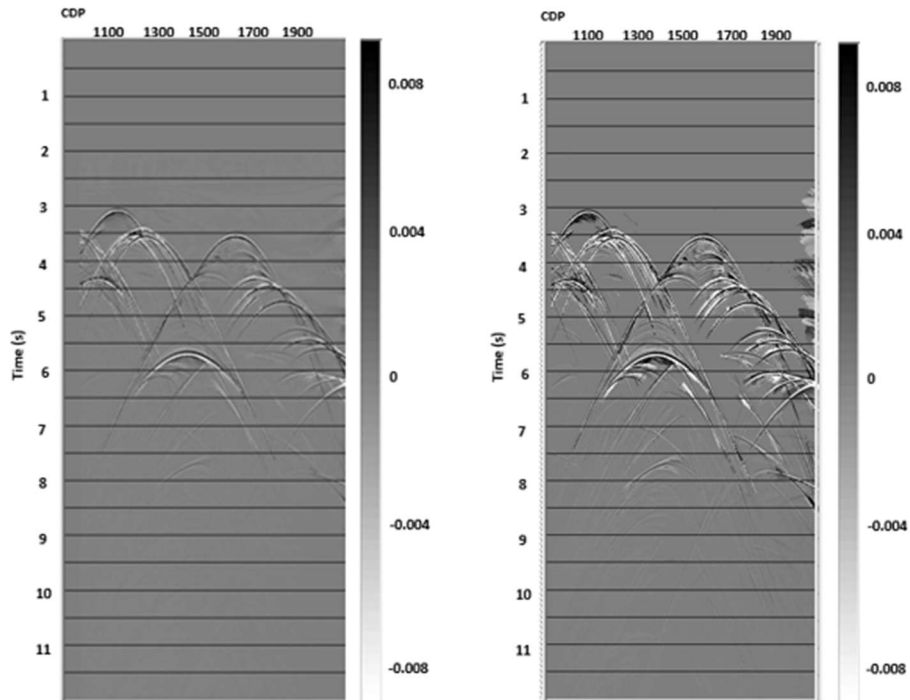


Figure C-2: DSR stack after thresholding for apertures Δm 1200 and Δh 500 («Endrias» on left and «Vemund» on right)

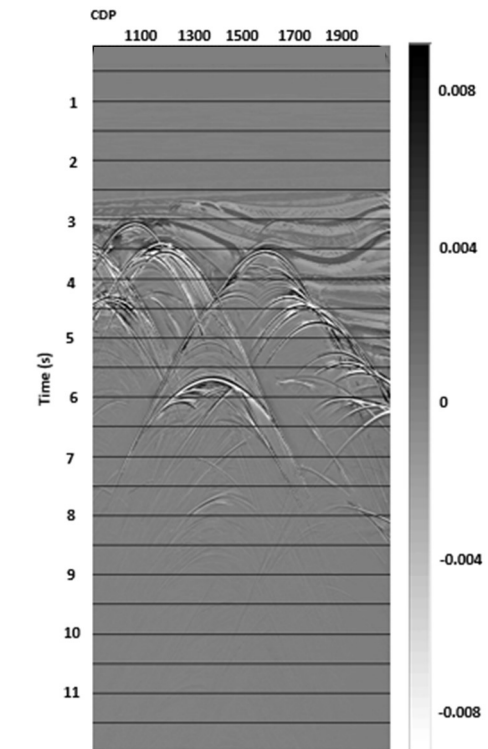


Figure C-3: DSR stack before thresholding for apertures Δm 800 and Δh 500

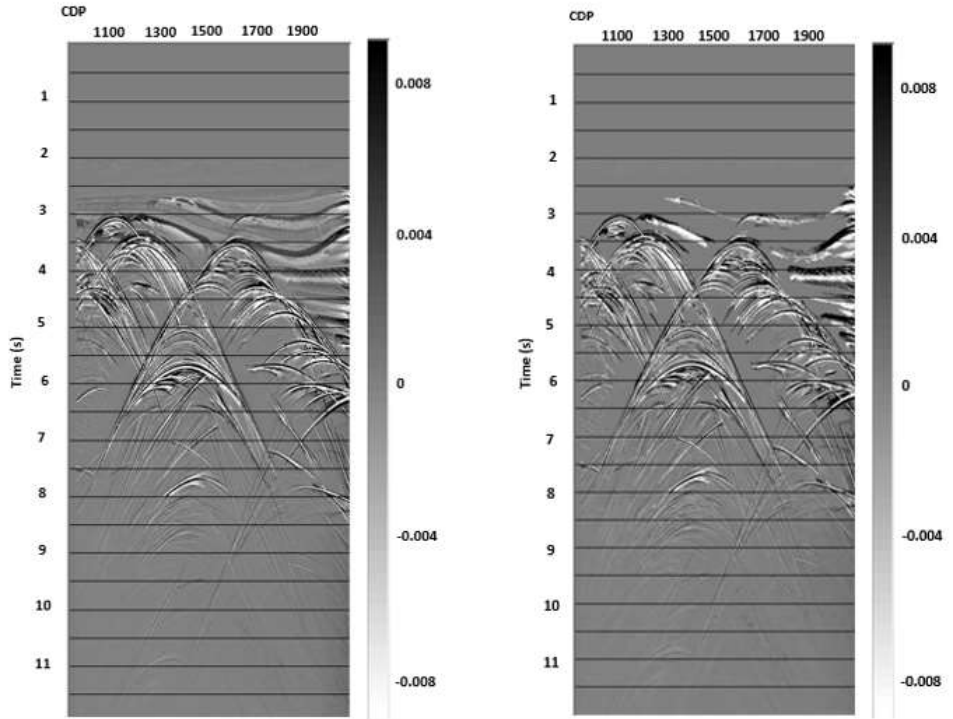


Figure C-4: DSR stack after thresholding for apertures Δm 800 and Δh 500 («Endrias» on left and «Vemund» on right)